Ab initio and molecular dynamics predictions for electron and phonon transport in bismuth telluride

Bao-Ling Huang and Massoud Kaviany*
Department of Mechanical Engineering, University of Michigan, Ann Arbor, Michigan 48109-2125, USA
(Received 7 December 2007; revised manuscript received 1 February 2008; published 12 March 2008; publisher error corrected 18 March 2008)

Phonon and electron transport in Bi_2Te_3 has been investigated using a multiscale approach, combining the first-principles calculations, molecular dynamics (MD) simulations, and Boltzmann transport equations (BTEs). Good agreements are found with the available experimental results. The MD simulations along with the Green-Kubo autocorrelation decay method are used to calculate the lattice thermal conductivity in both the in-plane and cross-plane directions, where the required classical interatomic potentials for Bi_2Te_3 are developed on the basis of first-principles calculations and experimental results. In the decomposition of the lattice thermal conductivity, the contributions from the short-range acoustic and optical phonons are found to be temperature independent and direction independent, while the long-range acoustic phonons dominate the phonon transport with a strong temperature and direction dependence (represented by a modified Slack relation). The sum of the short-range acoustic and optical phonon contribution is about 0.2 W/m K and signifies the limit when the long-range transport is suppressed by nanostructure engineering. The electrical transport is calculated using the full-band structure from the linearized augmented plane-wave method, BTE, and the energy-dependent relaxation-time models with the nonparabolic Kane energy dispersion. Temperature dependence of the energy gap is found to be important for the prediction of electrical transport in the intrinsic regime. Appropriate modeling of relaxation times is also essential for the calculation of electric and thermal transport, especially in the intrinsic regime. The maximum of the Seebeck coefficient appears when the chemical potential approaches the band edge and can be estimated by a simple expression containing the band gap. The scatterings by the acoustic, optical, and polar-optical phonons dominate the electrical conductivity and electric thermal conductivity.

DOI: 10.1103/PhysRevB.77.125209 PACS number(s): 63.20.−e, 72.15.Jf, 71.20.−b

I. INTRODUCTION

Efficient solid state energy conversion devices based on the thermoelectric (TE) effects, i.e., the Peltier effect for cooling and the Seebeck effect for power generation, have great application potential and economic benefits in many areas. However, present TE devices have a very low efficiency, which is directly limited by the performance of TE materials. The search into the fundamentals and improvement in TE transport phenomena continues. The performance of TE materials is presented by the dimensionless figure of merit (ZT),

$$ZT = \alpha_S^2 \sigma_e T/(k_e + k_p), \tag{1}$$

where α_S is the Seebeck coefficient, σ_e is the electrical conductivity, T is the temperature, and k_e and k_p are the electric and lattice thermal conductivities, respectively. Identifying and designing materials with high ZT has proven to be very challenging. Currently, the best bulk commercial TE materials for applications near room temperature are still the compounds based on Bi_2Te_3, with ZT near 1. Bi_2Te_3 exhibits many typical features of a good room-temperature TE material, such as a narrow band gap, high density of states near the band edges, and low total thermal conductivity. Understanding phonon and electron transport in Bi_2Te_3 is important in the design and optimization of TE materials.

Bulk Bi_2Te_3 has a rhombohedral lattice structure that belongs to the space group D_{3d}^5 ($R\bar{3}m$) and contains five atoms along the trigonal axis in the sequence of Te1-Bi-Te2-Bi-Te1 (Fig. 1). At 293 K, the rhombohedral unit-cell parameters[1] are $a_R = 10.473$ Å and $\theta_R = 24.159°$, and the corresponding hexagonal unit-cell parameters are $a = 10.473$ Å and $c = 30.487$ Å. In the rhombohedral structure, the fractional coordinates for Te1 atoms are designated as $(\pm u, \pm u, \pm u)$ and

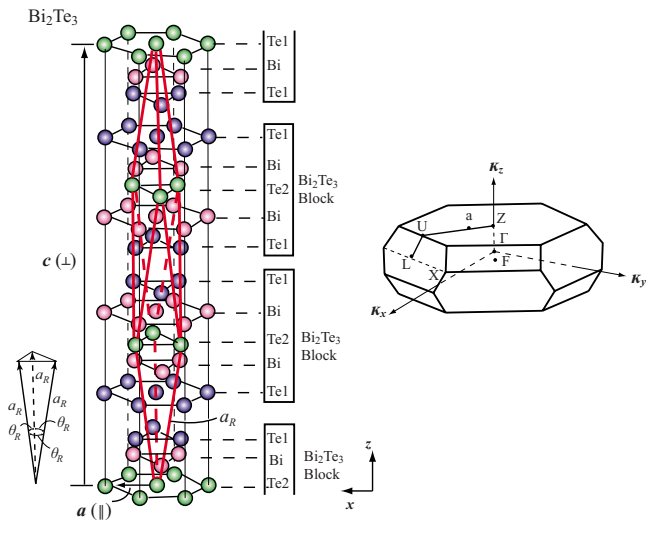

FIG. 1. (Color online) Crystal structure of Bi_2Te_3 showing both the rhombohedral and hexagonal unit cells. The first Brillouin zone for the rhombohedral cell and some symmetry axes and $\boldsymbol{k}$ points are also shown. The hexagonal structure is made of Te1-Bi-Te2-Bi-Te1 five-layer blocks.

those for Bi as $(\pm u, \pm v, \pm v)$, where u and v at 293 K have been found[2] to be 0.4001 and 0.2095. In the hexagonal unit cell (Fig. 1), it is apparent that Bi_2Te_3 has a lamella structure made of Te1-Bi-Te2-Bi-Te1 blocks. The bond length of the Te1-Bi bond is 3.07 Å shorter than that of the Bi-Te2 bond (3.25 Å), indicating that they may be of different bond types; the Te1-Te1 bond is the longest (3.64 Å) and is believed to be a van der Waals interaction, which responds to the ease of cleavage along the planes.[1,2] We denote the direction along the c axis (cross-plane direction) as "$\perp$" and the in-plane direction as "$\parallel$."

Significant experimental characterization efforts[1–9] on Bi_2Te_3 and some *ab initio* calculations and theoretical treatments[3,5,10] have been reported. However, theoretical treatments for both the phonon and electron transport in Bi_2Te_3 are rare, especially for the lattice thermal conductivity. The difficulty has been due to the different physical features of phonon and electron transport, and a multiscale approach is required for such investigations.

In order to systematically study the relationship between the TE properties and the structural features and to understand the transport mechanisms in TE materials, we develop a comprehensive strategy to calculate all the TE transport properties (α_S, σ_e, k_e, and k_p). In this strategy, first-principles calculations based on density functional theory (DFT), molecular dynamics (MD) simulations, and Boltzmann transport equation (BTE) are combined to calculate the TE transport properties of Bi_2Te_3. Below, we first report the classical interatomic potentials for Bi_2Te_3 developed on the basis of DFT energy calculations. With these potentials, the lattice vibrations are analyzed using MD simulations. Then, the lattice thermal conductivity along the in-plane and cross-plane directions are calculated in a temperature range from 150 to 450 K using MD combined with the Green-Kubo (GK) autocorrelation decay method. For an electric transport, we start with the first-principles band structure calculations and the modeling for the chemical potential. Then, the electric transport properties (α_S, σ_e, and k_e) are determined using BTE with the appropriate modeling of the relaxation time and chemical potential between 100 and 500 K. The calculated results are in reasonable agreement with the experiments, noting that the experiments inherently contain various defects.

II. PREDICTION OF PHONON CONDUCTIVITY

There are two common theoretical approaches in the investigation of phonon transport in solids. One is the continuum transport theory (or kinetic theory), such as BTE,[11,12] which is suitable for fast calculations of large systems. However, this normally needs some parameter input from experiments or other predictions; therefore, its application is limited. The other is the atomistic technique, such as MD simulations. Unlike BTE, MD only requires material structures and suitable interatomic potentials. In a sense, MD is more fundamental and can provide insight into the lattice dynamics at the atomic level. Also, MD allows for decomposing different transport mechanisms and is therefore chosen here.

A. Interatomic potentials

Suitable interatomic potentials are essential for modeling the lattice dynamics of Bi_2Te_3 in the MD simulations. Though there are already some simple harmonic potentials fitted using the experiments in the literature,[3,5] they are not suitable for the calculation of lattice conductivity due to the omitted anharmonic effects. Here, the interatomic potentials involving the anharmonic terms have been developed by fitting the energy surface from the *ab initio* calculations. The *ab initio* energy surface scan is normally carried out by considering only small isolated clusters. This approach is valid only when the interatomic interactions in a real crystal are mainly of short range. However, long-range interactions, e.g., van der Waals interactions, may be important in determining the structure and dynamics of Bi_2Te_3.[3] Therefore, a crystal structure with a periodic boundary condition was adopted in the energy surface scan.

The *ab initio* calculations were performed with the QUANTUM-ESPRESSO package[13] within the DFT framework using a plane-wave basis set and pseudopotentials adopting the Ceperley-Alder local density approximation (LDA) with Perdew-Zunger data. A cutoff energy of 50 Ry was used, and the spin-orbit coupling was included. The energy surface of Bi_2Te_3 was scanned by changing the bond lengths and angles. Both a rhombohedral primitive cell and a hexagonal representation were used in the scan. The classical potentials with predetermined forms were first fitted to these data using the GULP code.[14] Then, the crystal structure and other properties such as the elastic constants were calculated by implementing those potentials in the GULP package and compared with experimental results. Such procedures iterated until convergent results were achieved. Note that the DFT with the generalized-gradient approximation (GGA) or LDA cannot describe the true long-range van der Waals interactions.[15] Though recent developments[15] have seamlessly included van der Waals interactions in DFT, the solutions are not very simple and are unavailable in most present DFT codes. In this work, the van der Waals interactions were first parametrized by fitting the energy surface scanned by QUANTUM-ESPRESSO and subsequently refined by fitting to the structure and elastic constants. In the fitting with the energy surface, we adopted the atomic charges fitted by Kullmann *et al.*[5] The final forms of the interatomic potentials are listed in Table I.

It is interesting to note that the Te1-Bi bond has a higher bond energy and a higher force constant than the Te2-Bi bond. Also, its potential has a larger spatial variation than the Te2-Bi bond, showing a stronger bond anharmonicity. This indicates that the Te1-Bi bond is more ionic than the Te2-Bi bond. The Te1-Te1 bond, which is commonly considered as a van der Waals interaction, has a bond energy $\varphi_o = 0.0691$ eV, lower than that of a typical ionic or covalent bond but much higher than the bond energy of the Xe-Xe or Kr-Kr van der Waals interaction (for Xe-Xe, $\varphi_o = 0.014$ eV, and for Kr-Kr, $\varphi_o = 0.02$ eV),[16] which has a close filled-shell atomic radius. Also, the force constant Γ of Te1-Te1 at the equilibrium site is 10.45 N/m, which is also much larger than those of Xe-Xe ($\Gamma = 0.96$ N/m) and Kr-Kr ($\Gamma = 1.15$ N/m).[16] This value agrees well with the results of Jenkins *et al.*[3] ($\Gamma = 9.83$ N/m) and Kullmann *et al.*[5]

TABLE I. The interatomic potentials (excluding the electrostatic interactions) for Bi_2Te_3. Here, r and θ are the interatomic separation distance and bond angle, respectively. The cutoff radius of the electrostatic terms is 12 Å. The atomic charges of Te1, Bi, and Te2 are −0.26, 0.38, and −0.24, respectively (Ref. 5).

Interaction	Potential Model	Parameters
Pair		
Te1-Bi (adjacent layers)	$\varphi_o\{[1-\exp(-a(r-r_o))]^2-1\}$	φ_o=0.974 eV, a=1.2848 Å^{-1}, r_o=3.10 Å
Te2-Bi (adjacent layers)	$\varphi_o\{[1-\exp(-a(r-r_o))]^2-1\}$	φ_o=0.5801 eV, a= 1.2537 Å^{-1}, r_o= 3.235 Å
Te1-Te1 (adjacent layers)	$\varphi_o\{[1-\exp(-a(r-r_o))]^2-1\}$	φ_o=0.0691 eV, a= 2.174 Å^{-1}, r_o=3.64 Å
Bi-Bi (same layer)	$\varphi_o\{[1-\exp(-a(r-r_o))]^2-1\}$	φ_o=0.085 eV, a= 1.93 Å^{-1}, r_o=4.18 Å
Angular		
Te1-Bi-Te1 (adjacent layers)	$\frac{1}{2}\varphi_\theta(\cos\theta-\cos\theta_o)^2$	φ_θ=0.56 eV, θ_o=90°
Bi-Te1-Bi (adjacent layers)	$\frac{1}{2}\varphi_\theta(\cos\theta-\cos\theta_o)^2$	φ_θ=1.31 eV, θ_o=90°
Te2-Bi-Te2 (adjacent layers)	$\frac{1}{2}\varphi_\theta(\cos\theta-\cos\theta_o)^2$	φ_θ=1.47 eV, θ_o=85°
Bi-Te2-Bi (adjacent layers)	$\frac{1}{2}\varphi_\theta(\cos\theta-\cos\theta_o)^2$	φ_θ=1.47 eV, θ_o=85°
Te2-Bi-Te1 (three adjacent layers)	$\frac{1}{2}\varphi_\theta(\cos\theta-\cos\theta_o)^2$	φ_θ=1.16 eV, θ_o=92°
Bi-Te2-Bi (three adjacent layers)	$\frac{1}{2}\varphi_\theta(\cos\theta-\cos\theta_o)^2$	φ_θ=1.18 eV, θ_o=95°

(7.98 N/m). The large bond energy, the force constants, and the large spatial variation of the Te1-Te1 interaction indicates that the Te1-Te1 (excluding electrostatic interaction) interaction may be special. As will be discussed in Sec. III A, the interatomic bonds in each quintuple layer are primarily the $pp\sigma$ interactions.

We applied these potentials in the GULP package to optimize the structure (energy minimization). The resulting c and a values at 0 K are listed in Fig. 2, compared with the values measured[17] at 4 K. Since structure parameters at low temperatures are unavailable, we also used MD to obtain the average bond lengths and angles in a freestanding structure at 300 K, and the comparisons with the experimental results measured[1,2] at 293 K are shown in Fig. 2. The overall agreement is good (the average deviation from the measured data is less than 1%). The calculated Te1-Te1 bond length at 0 K (not shown) in the crystal is 3.62 Å, shorter than the equilibrium bond length parameter 3.64 Å listed in Table I. This indicates that the repulsion between the adjacent two Te1 layers is overwhelmed by the electrostatic interaction between the distant Bi and Te1 layers in two neighboring blocks. However, at high temperature, as shown in Fig. 2, the attraction between the two adjacent Te1 layers originates from both the electrostatic interaction and the weak Te1-Te1 bonds. The combination of the electrostatic interaction and the strong van der Waals interaction makes the net Te1-Te1 interaction behave as an ionic bond.

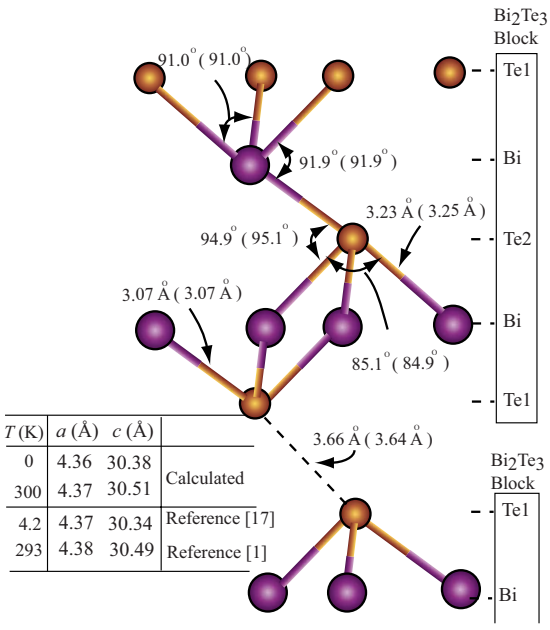

FIG. 2. (Color online) Comparison of the structure parameters calculated by the model at 300 K with those (Refs. 1 and 17) (shown in the parentheses) from experiments at 293 K. The calculated lattice parameters at 0 and 300 K, together with the experimental results (Refs. 1 and 17), are also shown.

The elastic constants (the elastic modula $C_{\alpha\beta}$, bulk modulus E_p, and Young modulus E_Y) of the optimized structure are also calculated using the dynamical matrix approach implemented in the GULP package. In performing the lattice dynamical calculation, the Cartesian reference axis is chosen to be the same as that in Ref. 3. The calculated results apply to 0 K. Table II compares the elastic constants of the optimized structure with the experimental data at different temperatures.[3,5] Except for $C13$, our data for the optimized structure at 0 K agree quite well with the elastic constants at 0 K measured by Jenkins *et al.*,[3] and the average deviation from the measured values is less than 10%. We also calculate the elastic constants of a freestanding structure at 300 K. As shown in Table II, the changes of the elastic constants $\Delta C_{\alpha\beta}$ agree quite well with the experiments. This indicates that these potentials can be used to describe the harmonic behaviors of Bi_2Te_3 over a wide temperature range. Also, note that $C11$ is only slightly larger than $C33$ because of the high force constant of Te1-Te1 bonds, which shows weak anisotropy in the elastic properties of the layered Bi_2Te_3 structure.

The umklapp processes, in which the phonon momentum is changed by a reciprocal lattice vector, dominate the lattice

TABLE II. Comparison of the calculated elastic modula $C_{\alpha\beta}$, bulk modulus E_p, and in-plane Young modulus E_Y (in GPa) with experimental results (Refs. 3 and 5).

	C_{11}	C_{13}	C_{14}	C_{33}	C_{44}	C_{66}	E_p	E_Y
Ultrasonic experiment (280 K)[a]	68.5	27.0	13.3	47.7	27.4	23.4	37.4	54.2
Ultrasonic experiment (0 K)[a]	74.4	29.2	15.4	51.6	29.2	26.2	39.5[b]	
Neutron scattering experiment (77 K)[5]	76.3		13.2	51.2	30.9	9.9		
This study (0 K)	69.0	21.6	12.3	54.8	28.8	26.7	34.4	52.5
This study (300 K)	65.4	19.0	10.9	50.7	26.5	25.7	31.6	51.4

[a]Reference 3.
[b]calculated through the bulk modulus relation in Ref. 3.

thermal conductivity of crystalline materials at normal and high temperatures (typically above 1/3–1/2 of the Debye temperature). This intrinsic resistive process results from the anharmonicity of the interatomic potentials in solids. Its strength depends on both the available phonon phase and the phonon-phonon scattering matrix, which are, in turn, determined by the harmonic force constants and anharmonicity of the interatomic potentials, respectively.[18] Therefore, we chose the Grüneisen parameter and the linear thermal expansion coefficients to check the anharmonicity of the interatomic potentials before applying them in the thermal conductivity calculations.

The mode Grüneisen parameter $\gamma_{G,\boldsymbol{\kappa},s}$ describes the relative shift of phonon frequency of the mode ($\boldsymbol{\kappa}$, s) with the change of the volume and is defined as

$$\gamma_{G,\boldsymbol{\kappa},s} = -\frac{V}{\omega_s(\boldsymbol{\kappa})}\frac{\partial \omega_s(\boldsymbol{\kappa})}{\partial V}, \tag{2}$$

where the mode is denoted by the wave vector $\boldsymbol{\kappa}$ and the branch identifier s, ω is the angular frequency, and V is the volume. The overall Grüneisen parameter is defined as

$$\gamma_G = \frac{\Sigma_{\boldsymbol{\kappa},s}\gamma_{\boldsymbol{\kappa},\alpha}c_{v,s}(\boldsymbol{\kappa})}{\Sigma_{\boldsymbol{\kappa},s}c_{v,j}(\boldsymbol{\kappa})},$$

$$c_{v,s}(\boldsymbol{\kappa}) = \frac{\hbar\omega_s(\boldsymbol{\kappa})}{V}\frac{\partial}{\partial T}\left[\frac{1}{e^{\hbar\omega_s(\boldsymbol{\kappa})/k_BT}-1}\right] = \frac{\beta E_p}{c_v}, \tag{3}$$

where $c_{v,s}(\boldsymbol{\kappa})$ is the contribution of the mode ($\boldsymbol{\kappa}$, s) to the volumetric specific heat c_v, and β is the volumetric thermal expansion coefficient. To calculate the volume dependence of the phonon frequencies in Eq. (2), we used GULP to calculate the volume of a hexagonal unit cell under different hydrostatic pressures p by minimizing the enthalpy of the system. With the resulting structure, the phonon frequency at each $\boldsymbol{\kappa}$ point was recalculated by diagonalizing the corresponding dynamical matrix (a $6\times6\times6$ $\boldsymbol{\kappa}$ mesh was used). The Grüneisen parameter was then calculated from the changes in the phonon frequencies and listed in Table III.

The linear thermal expansion coefficient β_α was obtained from the elastic compliance coefficient S_{ij} and from the generalized Grüneisen parameters, which are defined as[19]

$$\gamma'_{G,\alpha} = \frac{\Sigma_{\boldsymbol{\kappa},s}\gamma'_{\alpha,\boldsymbol{\kappa},s}c_{v,s}(\boldsymbol{\kappa})}{\Sigma_{\boldsymbol{\kappa},s}c_{v,s}(\boldsymbol{\kappa})}, \quad \gamma'_{G,\alpha,\boldsymbol{\kappa},s} = -\frac{1}{\omega_s\boldsymbol{\kappa}}\frac{\partial\omega_s(\boldsymbol{\kappa})}{\partial\epsilon_\alpha}, \tag{4}$$

where ϵ_α is a uniform areal strain along the α direction. The linear thermal expansion coefficients of a hexagonal crystal can be obtained from[19]

$$\beta_\parallel = [(S_{11}+S_{12})\gamma'_\parallel + S_{13}\gamma'_\perp]c_v, \tag{5}$$

$$\beta_\perp = [2S_{13}\gamma'_\parallel + S_{33}\gamma'_\perp]c_v. \tag{6}$$

The corresponding volumetric thermal expansion coefficient β is

$$\beta = 2\beta_\parallel + \beta_\perp. \tag{7}$$

The calculated results and those from experiments at $T=300$ K are also listed in Table III.

From Table III, the calculated anharmonic properties agree well with the experimental results. Therefore, we would expect this set of interatomic potentials to provide a reasonable prediction for the lattice thermal conductivities.

Since Bi_2Te_3 is a highly anisotropic layered structure, to characterize the anharmonicities along different polarizations, similar to Eq. (3), we can also define a polarized Grüneisen parameter,

TABLE III. Comparison of the calculated Grüneisen parameters and thermal expansion coefficients, at $T=293$ K, with the experimental results (Refs. 1, 3, and 20).

Parameter	γ_G	$\gamma_{G,\parallel}$	$\gamma_{G,\perp}$	β (10^{-6}/K)	$\beta_\parallel$ (10^{-6}/K)	$\beta_\perp$ (10^{-6}/K)
Experiment	1.49[3]			48.0,[a] 44.0[b]	12.9,[a] 13.0[b]	22.2,[a] 18.0[b]
Calculation	1.40	1.17	1.86	46.8	12.9	21.0

[a]Reference 1.
[b]Reference 20.

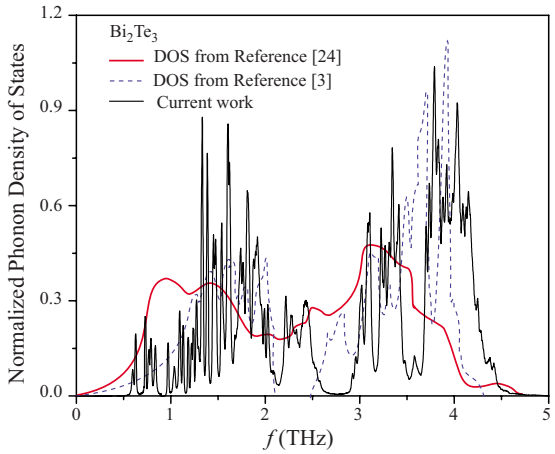

FIG. 3. (Color online) Predicted variation of the normalized phonon DOS for Bi_2Te_3 with respcet to frequency, and the comparison with the available DOS (Refs. 3 and 24).

$$\gamma_{G,\alpha} = \frac{3\beta_\alpha E_p}{c_v}, \tag{8}$$

which measures the anharmonicity along the α direction and equates to γ_G if the structure is isotropic ($\gamma_G = \Sigma_\alpha \gamma_{G,\alpha}/3$). Table III shows that the in-plane Grüneisen parameter $\gamma_{G,\parallel}$ is close to the γ_G value of an ideal covalent material[21] and is much smaller than the cross-plane Grüneisen parameter $\gamma_{G,\perp}$, indicating that the in-plane anharmonic scattering is much weaker than the cross-plane anharmonic scattering. The calculated $\gamma_{G,\perp}$, however, is a typical value of an ionic material, which confirms the conclusion about the Te1-Te1 ioniclike mixed bond.

B. Lattice vibrations

To further investigate the lattice vibrations of Bi_2Te_3, we also used the MD simulations to calculate the normalized total phonon density of states (DOS) [Fig. 3(a)] together with the atomic partial phonon density of states (PDOS) (Fig. 4). The normalized PDOS of the βth species in the α direction, $D^*_{p,\beta,\alpha}$, is determined by taking the Fourier transform of the velocity autocorrelation function (1800 ps raw velocity data were used in the autocorrelation calculation),[22,23]

$$D^*_{p,\beta,\alpha}(\omega) = \frac{\int \exp(-i\omega t)\langle u_{\beta,\alpha}(t)u_{\beta,\alpha}(0)\rangle dt}{\int\int \exp(-i\omega t)\langle u_{i,\beta,\alpha}(t)u_{i,\beta,\alpha}(0)\rangle dt d\omega}, \tag{9}$$

where $u_{\beta,\alpha}$ denotes the velocity of an atom of the βth species in the α direction.

The normalized total phonon DOS is obtained by summing over the normalized partial DOS weighted with the species concentration c_β,

$$D^*_p(\omega) = \sum_{\beta,\alpha} c_\beta D^*_{p,\beta,\alpha}(\omega). \tag{10}$$

To obtain the DOS and PDOS, the MD simulations were run at 300 K, and 1800 ps raw velocity data were used in the

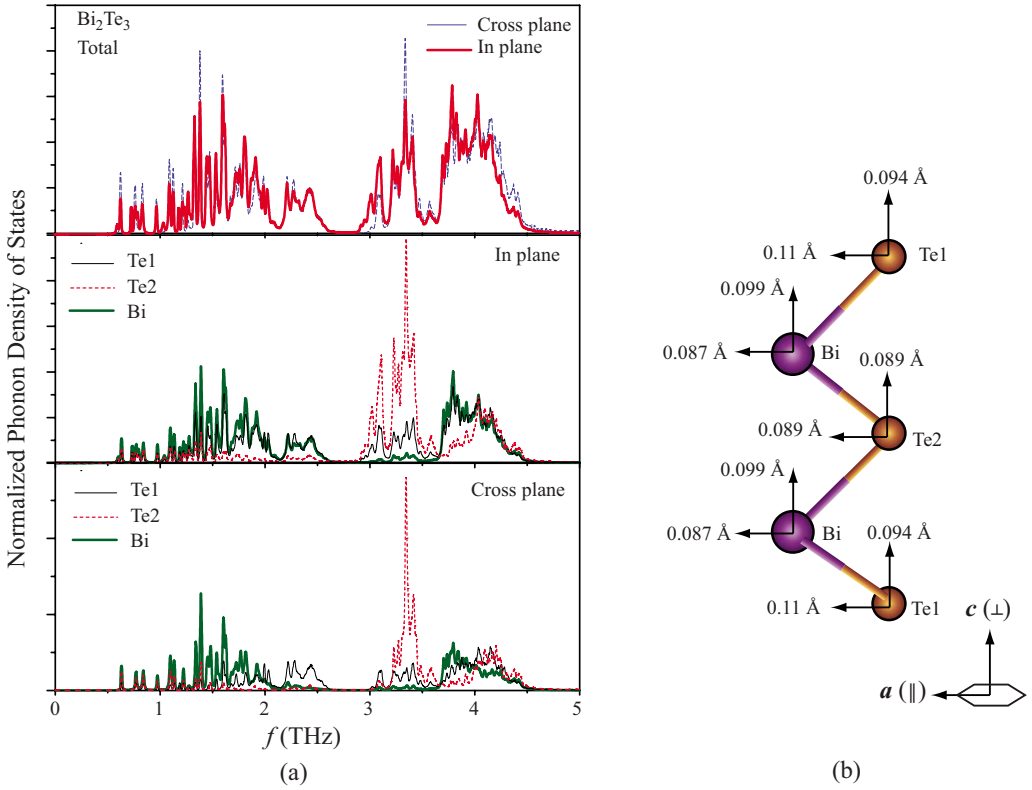

FIG. 4. (Color online) (a) Predicted variation of the directional phonon DOS for Bi_2Te_3 with respect to frequency. (b) Root mean square of the displacement for various atoms in Bi_2Te_3.

calculation for the autocorrelation function. The obtained total phonon DOS is shown in Fig. 3. The generalized phonon density of states $G(\omega)$ measured at 77 K by Rauh *et al.*[24] using the inelastic neutron scattering and that calculated by Jenkins *et al.*[3] with the assumed Born–von Karman model are also shown in Fig. 3. Note that the $G(\omega)$ measured by Rauh *et al.*[24] is not the conventional DOS because the difference of the weight factors is significant for Bi and Te. The cutoff frequency calculated by the MD simulation is 4.7 THz, larger than the value of 4.3 THz calculated by Jenkins *et al.*[3] but agreeing well with the value of 4.7 THz measured by Rauh *et al.*[24] and of 4.55 THz measured by Kullmann *et al.*[5] Overall, our DOS results agree fairly well with that of Jenkins *et al.*[3] In our DOS results, there is a gap between 2.5 and 2.9 THz, which is mainly determined by the weak Te1-Te1 bond and the Te2-Bi bond. Neither our model nor that of Jenkins *et al.*[3] can reproduce the transversal eigenmode around 1.0 THz. This may be due to the simple nature of the "rigid-ion" model since the high polarizability of Te and Bi may significantly influence the dispersion behavior of the transverse optical mode. A suitable core-shell model may account for this problem, which will be investigated in the future.

Figure 4(a) shows the normalized in-plane and cross-plane phonon DOSs of the entire Bi_2Te_3 structure and those of the different species. Overall, the in-plane and cross-plane phonon DOSs almost overlap, especially when $f<3$ THz, and the difference only lies in the high-frequency regime ($f>3$ THz), where the cross-plane spectrum seems to shift a little toward a relative higher frequency regime. This rough identity indicates that there is only a minor difference between the in-plane and cross-plane vibration spectra, which is consistent with the fact that $C11$ differs only slightly from $C33$. The in-plane and cross-plane PDOSs of the different species provide more details about the lattice vibration. When $f<1.5$ THz, where acoustic vibrations dominate, the three PDOSs for both directions are almost the same. The Bi atoms have more modes in the low-frequency regime ($f<2.6$ THz) of the PDOS for both directions, but less modes in the high-frequency regime ($f>3$ THz) than those of the Te1 and Te2 atoms. This is due to their larger mass. Overall, the in-plane PDOSs of Te1 and Bi match each other quite well, and the difference only exists in a narrow frequency regime (2.8 THz$<f<$3.6 THz). This is believed to directly result from the strong Te1-Bi bonds. However, most in-plane vibration modes of Te2 atoms concentrate in the high-frequency regime (2.8 THz$<f<$4.6 THz). The in-plane vibration spectrum of Te1 shows strong peaks between 2.8 and 3.6 THz, where Te1 and Bi have much less vibration modes. Te2 also has much less vibration modes than Bi and Te1 atoms in the regime between 1.5 and 2.6 THz. All these show that the correlation between the in-plane optical vibrations of Te2 and Bi/Te1 is weak, while the correlation between the in-plane vibrations of Bi and Te1 is strong. This may be due to the relatively weak Bi-Te2 bonds (compared with Bi-Te1 bonds) and the symmetric position of Te2 atoms in the five-layer sandwich structure. Similarly, the cross-plane PDOS of Te2 atoms mainly focuses on the high-frequency regime ($f>2.8$ THz). There are strong peaks between 3 and 3.6 THz in the cross-plane PDOS of Te2, but those peaks are rather weak in the PDOS of Te1 and Bi, indicating the energy localization of those modes. Also, there are large differences among the cross-plane PDOSs of neighboring Te1/Bi and Bi/Te2 layers, suggesting that phonon transporting across the planes will suffer from strong scattering. Those strong scatterings are mainly due to the mass difference and the large variation in $\Gamma\gamma'$ ($\Gamma\gamma'$ is the product of the force constant Γ and the bond-scaling parameter γ') in the neighboring bonds.[21] Figure 4(b) shows the root mean square (rms) displacement of atoms. The rms' of the Te2 atoms are isotropic, while the Bi atoms have the largest cross-plane rms and the Te1 atoms have the largest in-plane rms.

C. Molecular dynamics simulation procedure and GK autocorrelation

The thermal conductivity limited by the phonon-phonon scattering $\boldsymbol{K}_p$ is determined using the GK approach, in which the thermal conductivity is related to the decay of the heat current autocorrelation function (HCACF). The thermal conductivity $\boldsymbol{K}_p$ tensor is given by

$$\boldsymbol{K}_p = \frac{1}{k_B V T^2}\int_0^\infty \langle \dot{\boldsymbol{w}}(t)\dot{\boldsymbol{w}}(0)\rangle, \tag{11}$$

where k_B is the Boltzmann constant, V is the volume of the simulation system, T is the system temperature, and $\langle \dot{\mathbf{w}}(t)\cdot\dot{\mathbf{w}}(0)\rangle$ is the HCACF. A slow-decaying HCACF indicates that the heat current fluctuations can spread over a long time before vanishing, i.e., a long phonon relaxation time. The heat current $\dot{\boldsymbol{w}}$ is defined as

$$\dot{\boldsymbol{w}} = \frac{d}{dt}\sum_{i=1}^{N} \boldsymbol{r}_i E_i, \tag{12}$$

where $\boldsymbol{r}$ and E are the position vector and the energy of a particle (atom) (excluding the site energy), respectively.

The MD simulations were performed with a system consisting of $6\times6\times1$ hexagonal unit cells and involving 540 atoms. The simulations with larger systems produced very similar results. The temperatures considered were from 100 to 400 K, with an interval of 50 K. The time step was chosen as 10 fs. The Verlet leapfrog algorithm was adopted for the calculation, while the Nose-Hoover thermostat and the Berendsen barostat were used to control the system temperature and pressure. The system was first simulated in an *NPT* (constant number of atoms, pressure, and temperature) ensemble for 100–200 ps until it reached a freestanding state at the desired temperature; then, it was switched into an *NVE* ensemble and ran for 200 ps to arrive in equilibrium. At each temperature point, 1700 ps raw heat current data were obtained for the calculation of HCACFs. After calculating HCACF, the direct integration method is used to obtain the thermal conductivity. The integral is averaged to smooth the behavior in a converged region. The final result is the average value over the converged region.

To speed up the calculations, the Wolf method[25] was adopted for the calculation of the long-range electrostatic

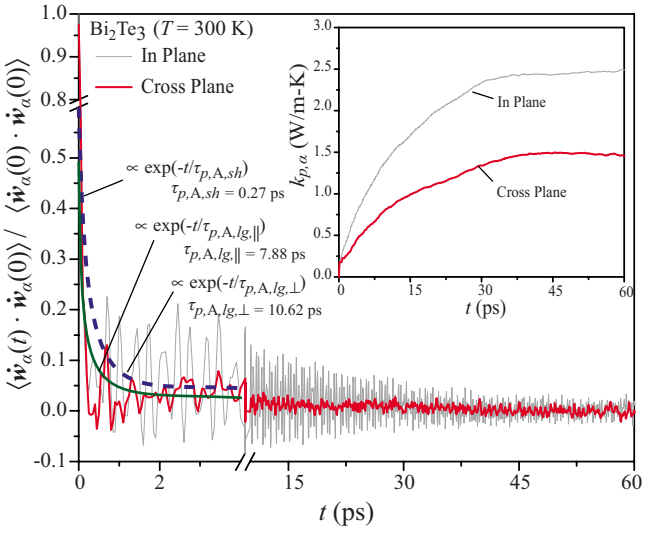

FIG. 5. (Color online) Time variation of the raw HCACF and the lattice thermal conductivity at $T=300$ K, for the in-plane and cross-plane directions. The curve fits of the two-term exponential functions for the HCACF low-frequency portion are also shown.

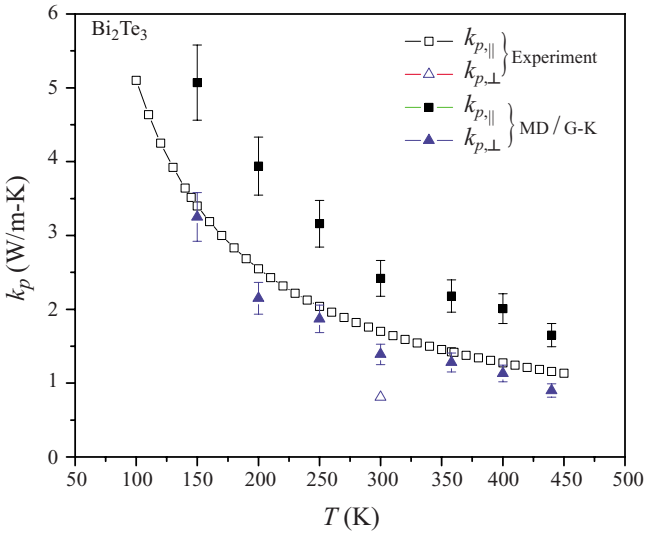

FIG. 6. (Color online) Predicted temperature-dependent in-plane and cross-plane lattice thermal conductivity, compared with the experimental results (Ref. 27).

interactions. The decay parameter β is chosen to be 0.25 Å^{-1}, and the cutoff radius R_c is chosen to be 10 Å.

D. Phonon conductivities and its decomposition

Figure 5 shows the time variation of the normalized raw HCACF and the lattice thermal conductivity along the in-plane and cross-plane directions. The normalization factors $\langle \dot{w}_\alpha(0)\cdot\dot{w}_\alpha(0)\rangle$ for the two directions only differ slightly ($<3\%$). The normalized raw HCACF curves in both directions involve high-frequency components caused by the high-frequency optical phonons. It is apparent that the fluctuations in the in-plane HCACF are much larger than those in the cross-plane one. Considering the identity of the normalized vibration spectrum along the two directions, the high-frequency vibrations along the cross-plane direction are more likely to be localized. Both HCACF curves consist of two stages, i.e., an initial rapid decay stage followed by a relatively slow decay stage, which have also been found for other crystals.[26] It has been shown that the HCACF of a crystal with a multiatom unit cell can be decomposed into three parts by fitting the HCACF to a function of the form[26]

$$\begin{aligned}\langle \dot{w}_\alpha(t)\cdot\dot{w}_\alpha(0)\rangle = {} & A_{A,sh,\alpha}\exp(-t/\tau_{p,A,sh,\alpha}) \\ & + A_{A,lg,\alpha}\exp(-t/\tau_{p,A,lg,\alpha}) \\ & + \sum_i B_{O,i,\alpha}\exp(-t/\tau_{p,O,i,\alpha})\cos(\omega_{p,O,i,\alpha}t),\end{aligned} \tag{13}$$

where $\tau_{p,i}$ is a time constant, the coefficients A and B represent the strength of a given mode, and the subscripts sh, lg, A, and O denote short-range, long-range, acoustic, and optical contributions, respectively. We used a Fourier low-pass filter (the cutoff frequency was set at 1.5 THz) to remove the high-frequency components of HCACF and fitted the low-frequency acoustic part using the two-term exponential functions. The fitting results are also shown in Fig. 5. At the beginning, the decay relaxation times for HCACF curves are almost the same, rather short (0.27 ps). However, for the long-range decay, the relaxation time for the in-plane HCACF is 10.62 ps, which is longer than that for cross-plane HCACF (7.88 ps), indicating that the lattice scattering along the cross-plane direction is stronger. The time variation of the lattice thermal conductivities shown in Fig. 5 also confirms this.

Figure 6 shows the temperature-dependent in-plane and cross-plane lattice conductivities of Bi_2Te_3 calculated by the MD simulations using the potentials listed in Table I. The available experimental results[27] are also shown. Note that the calculated in-plane and cross-plane $k_{p,\parallel}$, $k_{p,\perp}$ are higher than the experimental results. This is expected, considering the various defects (e.g., isotopes, displacements, lamellae, etc.) in a real Bi_2Te_3 crystal,[28] which will reduce the thermal conductivity.

The lattice conductivities in both directions roughly follow the $1/T$ law, similar to insulators. The calculated cross-plane thermal conductivity $k_{p,\perp}$ is lower than the in-plane $k_{p,\parallel}$. Since the average cross-plane sound velocity (1631 m/s) is very close to the in-plane sound velocity (1775 m/s), the difference between the two thermal conductivities is mainly due to the different anharmonicities along the two directions. This can be verified by the directional Grüneisen parameter $\gamma_{G,\alpha}$ along the α direction. For Bi_2Te_3, at 300 K, the in-plane Grüneisen parameter $\gamma_{G,\parallel}$ is 1.17, while the cross-plane Grüneisen parameter $\gamma_{G,\perp}$ is 1.86. The large difference in the anharmonicity originates from the unique bond characteristics in the layered structure (Fig. 1), in which the intralayer bonds are mainly covalent but the interlayer bonds are the hybrids of the electrostatic interaction and the van der Waals interaction.

Figure 5 illustrates the different decay stages and components of HCACF. According to Eqs. (11) and (13), the lattice

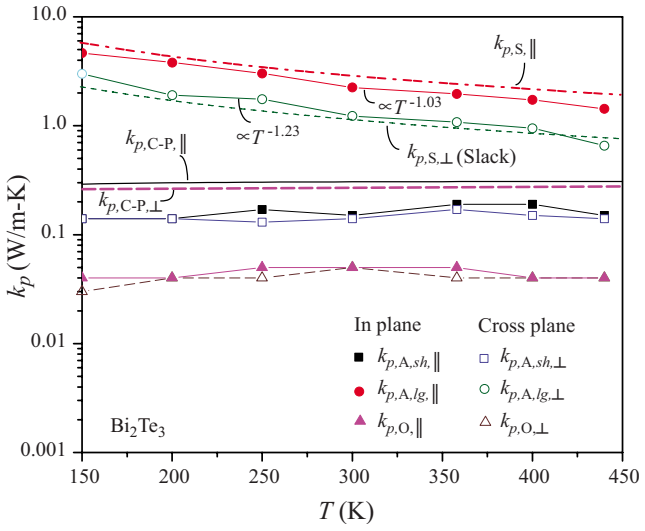

FIG. 7. (Color online) Decomposition of calculated in-plane and cross-plane thermal conductivity. The lowest in-plane and cross-plane thermal conductivities calculated by the Cahill-Pohl model are also shown.

thermal conductivity $\boldsymbol{K}_p$ can then be decomposed into three parts as

$$\boldsymbol{K}_p = \boldsymbol{K}_{p,A,sh} + \boldsymbol{K}_{p,A,lg} + \boldsymbol{K}_{p,O}. \tag{14}$$

Here, $\boldsymbol{K}_{p,lg,A}$ is believed to be the contribution from the long-range acoustic phonons, with a mean-free path larger than one-half of their wavelengths; $\boldsymbol{K}_{p,sh,A}$ is the contribution from the short-range phonons, with their mean-free paths minimized[26,29] (Kaburaki *et al.*[30] attributed it to single-particle motions in a local environment), and $\boldsymbol{K}_{p,O}$ is the contribution from the high-frequency optical phonons. We obtained $\boldsymbol{K}_{p,sh,A}$ and $\boldsymbol{K}_{p,lg,A}$ by fitting the low-frequency part of HCACF with the two-term exponential functions shown in Eq. (13) and obtained $\boldsymbol{K}_{p,O}$ by directly integrating the high-frequency part of HCACF. The Fourier low-pass and high-pass filters were used to separate the different components. Further details about the decomposition can be found elsewhere.[26,29]

Figure 7 shows the variation of the different components of the in-plane and cross-plane lattice thermal conductivities with respect to temperature. The results shown are the average for several data sets. The difference between the summation of the fitted three components and that specified directly from the integral is less than 10%. As shown in Fig. 7, for both the in-plane and cross-plane directions, the long-range contribution $k_{p,A,lg}$ dominates, and $k_{p,A,sh}$ is relatively small but still three to four times larger than $k_{p,O}$. The in-plane long-range contribution $k_{p,A,lg,\parallel}$ is larger than the cross-plane long-range component $k_{p,A,lg,\perp}$, and the ratio $k_{p,A,lg,\parallel}/k_{p,A,lg,\perp}$ varies from 1.55 to 2.17 in the temperature range 150–450 K. Considering the almost isotropic sound velocity and phonon DOS (Sec. II B), this difference is mainly attributed to the different scattering strengths along the two directions. However, the short-range and optical components are almost the same in both directions (the in-plane values seem slightly larger, but the difference is in the error range of the data). This seems to indicate that the mean-free paths of both the short-range and optical phonons are independent of the scattering mechanisms, and their transport is mainly determined by the local environment. This conclusion is consistent with the fact that $k_{p,A,sh}$ and $k_{p,O}$ are almost temperature independent. On the other hand, $k_{p,A,lg}$ decreases with increasing temperature. A power-law fit yields $k_{p,A,lg,\parallel} \propto T^{-1.03}$ and $k_{p,A,lg,\perp} \propto T^{-1.23}$, and the stronger temperature dependence of $k_{p,A,lg,\perp}$ may be due to the larger thermal expansion along the cross-plane direction. In other words, in both the in-plane and cross-plane directions, $k_{p,A,lg}$ roughly follows the normal T^{-1} law for high-temperature lattice thermal conductivities.

In Fig. 7, the lattice conductivity calculated by the Cahill-Pohl model[31] $k_{p,\mathrm{CP}}$ is also shown, which is given by

$$k_{p,\mathrm{CP}} = \left(\frac{\pi}{6}\right)^{1/3} k_B n^{2/3} \sum_{i=1}^{3} u_{p,g,i} \left(\frac{T}{T_{D,i}}\right)^2 \int_0^{T_{D,i}/T} \frac{x^3 e^x}{(e^x - 1)^2} dx, \tag{15}$$

where n is the number density of atoms. The lattice conductivity predicted by Eq. (15) has been interpreted as the minimum solid phase thermal conductivity. In Fig. 7, $k_{p,\mathrm{CP},\parallel}$ is only slightly higher than $k_{p,\mathrm{CP},\perp}$, and both are almost temperature independent in the temperature range between 150 and 450 K. The sum of $k_{p,A,sh}$ and $k_{p,O}$ is about 60% of $k_{p,\mathrm{CP},\parallel}$ or $k_{p,\mathrm{CP},\perp}$. The behaviors of $k_{p,A,sh}$ and $k_{p,O}$ are actually quite similar. If they are both mainly affected by a local environment, their sum seems likely to be independent of different scattering mechanisms unless the local environment (with a dimension of the order of the interatomic spacing) is changed. In other words, this provides a lower limit of the phonon conductivity for structure engineering, which is 0.2 W/m K at 300 K.

By assuming that heat was mainly carried by the acoustic phonons scattered via the three-phonon processes, Slack[32] proposed a simple relation for the thermal conductivity of crystals with constant volume at high temperatures

$$k_{p,S} = \frac{3.1 \times 10^4 \langle M \rangle N_c^{1/3} \delta T_{D,\infty}^3}{T \langle \gamma_G^2 \rangle}. \tag{16}$$

Here, $\langle M \rangle$ is the mean atomic weight of the atoms in the primitive cell, δ^3 is the average volume per atom, N_c is the number of atoms in a primitive cell, and $T_{D,\infty}$ is defined from the phonon DOS D_p,[32] i.e.,

$$T_{D,\infty}^2 = \frac{5h_P^2}{3k_B^2} \frac{\int_0^\infty f^2 D_p(f) df}{\int_0^\infty D_p(f) df}, \tag{17}$$

where h_P is the Planck constant and f is the phonon frequency. Note that the integral is only over the acoustic portion of the phonon spectrum. $T_{D,\infty}$ is generally close or slightly lower than the Debye temperature for the acoustic branches $T_D/N_c^{1/3}$ (T_D is the Debye temperature).

Slack mainly applied this relation for isotropic crystals with a cubic structure. However, as discussed in Ref. 21, if the long-range phonons dominate the heat transfer, their contribution may still have a form very similar to Eq. (16);

therefore, it is possible to modify this relation and apply it for anisotropic crystals. Assuming that the scattering of phonons along the α direction is only related to the elastic and anharmonic properties along this direction, that is, the transport of phonons along this direction is similar to the transport in an isotropic structure with the same elastic and anharmonic properties, then we extended Eq. (16) as

$$k_{p,S,\alpha} = \frac{3.1 \times 10^4 \langle M \rangle N_c^{1/3} \delta T_{D,\infty,\alpha}^3}{T \gamma_{G,\alpha}^2}, \quad \alpha = \perp \text{ or } \parallel. \tag{18}$$

Here, $T_{D,\infty,\alpha}$ is given by Eq. (17) while replacing $D_p(\nu)$ with $D_{p,\alpha}(\nu)$. As discussed in Sec. II B, the total in-plane and cross-plane PDOSs are almost the same, and the calculation according to Eq. (17) provides $T_{D,\infty,\parallel}=76$ K and $T_{D,\infty,\perp}=75$ K. Using $\gamma_{G,\parallel}=1.17$ and $\gamma_{G,\perp}=1.86$ calculated in Sec. II A, the in-plane and cross-plane long-range components [denoted as $k_{p,A,lg,\parallel}$ (Slack) and $k_{p,A,lg,\perp}$ (Slack)] were calculated by Eq. (18) and are also shown in Fig. 7. Overall, these results are in reasonable agreement with those decomposed from the MD simulations in both directions (the average deviations from the MD results are within 30% for $k_{p,A,lg,\parallel}$ and 20% for $k_{p,A,lg,\perp}$).

E. Role of phonon-electron scattering in phonon conductivity

In semiconductors, phonons are scattered by grain boundary, defects, other phonons, and carriers. According to the Matthiessen rule, the total thermal resisitivity can be represented as

$$\frac{1}{k_p} = \frac{1}{k_{p,b}} + \frac{1}{k_{p,d}} + \frac{1}{k_{p,U}} + \frac{1}{k_{p,c}}, \tag{19}$$

where $k_{p,b}$, $k_{p,d}$, $k_{p,U}$, and $k_{p,c}$ are the thermal conductivity limited by the scattering of grain boundary, defects, phonon-phonon U process, and carriers, respectively.

The thermal conductivity limited by phonon-carrier scattering $k_{p,c}$ can be estimated using the electrical resistivity ρ_e. Their relations have been derived by ignoring the difference between the N and U processes between carriers and phonons,[33,34] as in

$$\frac{1}{k_{p,c}} = \frac{A}{N_L T}\left(\frac{T_D}{T}\right) I_5 \frac{\pi^2 z_e^2}{27 I_4^2}, \tag{20}$$

$$\rho_e = A\left(\frac{T}{T_D}\right)^5 I_5, \tag{21}$$

where

$$I_n = \int_0^{T_D/T} \frac{x^n e^x}{(e^x-1)^2} dx. \tag{22}$$

In the above relations, z_e is the number of free electrons per atom, N_L the Lorenz constant, and A is a constant (for metals, $A=3.7$). Then, we have

$$\frac{1}{k_{p,c}} = \frac{\rho_e}{N_L T}\frac{(T_D/T)^6}{27 I_4^2}\pi^2 z_e^2. \tag{23}$$

When T/T_D increases from 0.1 to 10, $(T_D/T)^6/I_4(T_D/T)^2$ decreases from 97 to 9. Also, for a normal dopant concentration ($<10^{19}$ cm^{-3}), z_e is of the order of 10^{-3}. Then, for a wide temperature range ($0.1 \leqslant T/T_D \leqslant 10$), $1/k_{p,c}$ is only about 10^{-4} of the electrical thermal resistivity $1/k_e$ found from the Wiedemann-Franz law; therefore, it is negligible for most semiconductors (including Bi_2Te_3).

III. PREDICTION OF ELECTRONIC PROPERTIES

The thermoelectric transport properties can be derived from BTE with the relaxation time approximation. The general form of the relations for TE properties is[35]

$$\sigma_{e,\alpha\beta}(E_e) = \frac{1}{N}\sum_{i,\boldsymbol{\kappa}} e_c^2 \tau_{e,i,\boldsymbol{\kappa}} u_\alpha(i,\boldsymbol{\kappa}) u_\beta(i,\boldsymbol{\kappa}) \frac{\delta(E_e - E_{e,i,\boldsymbol{\kappa}})}{dE_e},$$

$$\sigma_{e,\alpha\beta} = \frac{1}{V}\int \sigma_{e,\alpha\beta}(E_e)\left[-\frac{\partial f_\mu(T;E_e)}{\partial E_e}\right] dE_e,$$

$$v_{\alpha\beta} = \frac{1}{e_c T V}\int \sigma_{e,\alpha\beta}(E_e)(E_e-\mu)\left[-\frac{\partial f_\mu(T;E_e)}{\partial E_e}\right] dE_e,$$

$$\alpha_{S,\alpha\beta} = (\sigma_e^{-1})_{j\alpha} v_{e,j\beta}$$

$$k^o_{\alpha\beta} = \frac{1}{e_c^2 T V}\int \sigma_{e,\alpha\beta}(E_e)(E_e-\mu)^2\left[-\frac{\partial f_\mu(T;E_e)}{\partial E_e}\right] dE_e,$$

$$k_{e,\alpha\beta} = k^o_{\alpha\beta} - T v_{\alpha j}(\sigma_e^{-1})_{lj} v_{l\beta}, \tag{24}$$

where α_S is the Seebeck coefficient, σ_e is the electrical conductivity, k_e is the electrical thermal conductivity, i is the band index, τ_e is the relaxation time, e_c is the charge of electron, $\boldsymbol{\kappa}$ is the wave vector, u is the group velocity, $f=[e^{(E_e-\mu)/(k_BT)}+1]^{-1}$ is the equilibrium Fermi-Dirac distribution function, μ is the chemical potential, and E_e is the total energy of electron. Accordingly, the band structure $E_e(i,\boldsymbol{\kappa})$, chemical potential μ, and relaxation times τ_e are required inputs for the electronic property calculations.

A. Electronic band structure of Bi_2Te_3

The band structure calculation for Bi_2Te_3 was carried out in the DFT framework. The WIEN2K Program,[36] which employs the full potential, linearized augmented plane-wave and local orbital methods, was chosen for this investigation. The GGA as proposed by Perdew *et al.*[37] was used for the exchange and correlation potential. The experimental rhombohedral cell parameters of $a=10.48$ Å and 24.16° and the atomic parameters[1,2] $u=0.4001$ and $v=0.2095$ at $T=300$ K were used in the calculations. The radii of both Bi and Te atoms were set at 2.8 a.u. An $\boldsymbol{R}\cdot\boldsymbol{\kappa}_{\max}$ value of 9 and a $G_{\max}$ value of 14 were adopted, and a nonshifted mesh with 10 000 $\boldsymbol{\kappa}$ points were used. The energy cutoff between the

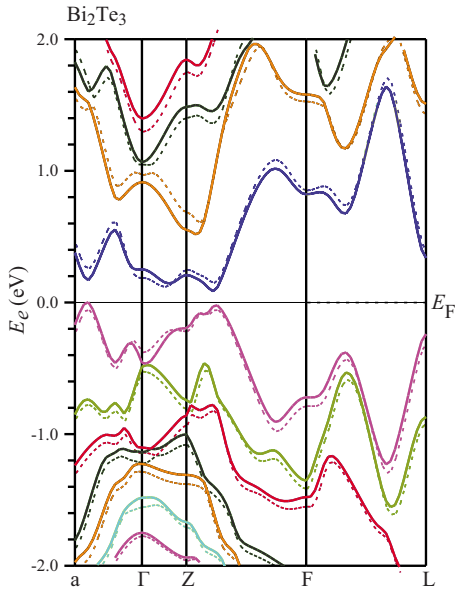

FIG. 8. (Color online) Electronic band structure of Bi_2Te_3 along the high-symmetry lines with spin-orbit coupling. The solid and dashed lines are for the results with and without the $p_{1/2}$ corrections included.

core and valence states was set at −6 Ry. Because of the significant spin-orbit (SO) effects on the band structure of Bi_2Te_3, the eigenstates below 10 Ry were considered in the SO calculations. As suggested by Larson,[38] the $p_{1/2}$ corrections may significantly affect the band structure; therefore, the $p_{1/2}$ corrections have also been considered for the Bi $6p$ and Te $5p$ states.

The calculated band structures along some high-symmetry lines is plotted in Fig. 8. The solid and dash lines show the results with and without the $p_{1/2}$ corrections, respectively. When the $p_{1/2}$ corrections are not included, our results are consistent with the results of Scheidemantel *et al.*[10] The band gap is evaluated as $\Delta E_{e,g}=0.13$ eV (Scheidemantel *et al.*[10] reported $\Delta E_{e,g}=0.11$ eV), which is slightly smaller than the zero-temperature experimental results[4] (0.16 eV). The band edges were found in the mirror plane and off the high-symmetry lines, yielding six highest valence bands and six lowest conduction bands (LCBs). The conduction band edge (CBE) is found at (0.667, 0.571, 0.571), close to those of previous investigations.[10,39,40] The secondary LCB edge is found at (0.238, 0.238, 0.238) with a 10 meV higher energy. The valence band edge (VBE) is also found at (0.667, 0.571, 0.571), the same $\boldsymbol{\kappa}$ position of the LCB edge. This result is close to (0.652, 0.579, 0.579) reported by Scheidemantel *et al.*,[10] but different from (0.546, 0.383, 0.383) found by Youn and Freeman[39] and (0.555, 0.397, 0.397) by Kim *et al.*[40] These comparisons are listed in Table IV.

As shown in Fig. 8, the addition of $p_{1/2}$ lowers the CBE but elevates the VBE, resulting in a decrease in $\Delta E_{e,g}$ from 0.13 to 0.07 eV. The positions of the band edges are still off the high-symmetry lines. The CBE remains at the same position (0.667, 0.571, 0.571), but VBE shifts to (0.571, 0.571, 0.429). Figure 8 also illustrates this shift.

The effective masses of electrons and holes for a single valley near the band edge $m^*_{i,e,o}=(m^*_{i,e,o,xx}m^*_{i,e,o,yy}m^*_{i,e,o,zz})^{1/3}$ $(i=e,h)$, where $m^{*\ -1}_{i,e,o,kl}=\hbar^{-2}[\partial^2 E_e/\partial\kappa_k\partial\kappa_l]$, were calculated by choosing a small region around the band extrema. As shown in Table IV, the addition of the $p_{1/2}$ corrections significantly reduces $m^*_{e,e,o}$ and $m^*_{h,e,o}$. Figure 9(a) also shows that the addition of the $p_{1/2}$ corrections lowers the slope of the electron density of states near the band edge. The band structure without the $p_{1/2}$ corrections seems to agree better with the experiments.[4,8,9]

The total electron density of states D_e with and without the $p_{1/2}$ corrections are shown in Fig. 9(a). It is apparent that D_e of both the valence bands and conduction bands are nonparabolic. However, we find that the Kane band structure model,[41] with $\Delta E_{e,g}$ and $m^*_{i,e,o}$ calculated from WIEN2K (listed in Table IV), gives a good approximation for D_e near both the conduction and valence band edges.

Many semiconductors with narrow band gap exhibit significant nonparabolicity of their energy bands. The two-band Kane model,[41] which has been used successfully to describe many real narrow gap materials,[7] was adopted to account for theoretical calculations of transport coefficients. The Kane model assumes that the band extrema for the conduction and valence bands are located at the same κ point. The energy separation from other bands is greater than the main energy gap, and the momentum operator has nonzero matrix elements between the states corresponding to the extremal points.[42] The dispersion relation of the bands of a valley is of the form

TABLE IV. Comparison of the calculated CBE, VBE, and the corresponding effective masses $m^*_{i,e,o}=(m^*_{i,e,o,xx}m^*_{i,e,o,yy}m^*_{i,e,o,zz})^{1/3}$ at the band edges, with the available results (Refs. 10 and 38–40).

Reference	$\Delta E_{e,g}$ (eV)	CBE	VBE	$m^*_{e,e,o}$	$m^*_{h,e,o}$
Youn and Freeman (Ref. 39)	0.06	(0.663, 0.568, 0.568)	(0.546, 0.383, 0.383)		
Larson (Ref. 38)	0.05	(0.381, 0.5, 0.5)	(0.546, 0.383, 0.383)		
Scheidemantel *et al.* (Ref. 10).	0.11	(0.663, 0.568, 0.568)	(0.652, 0.579, 0.579)		
Kim *et al.* (Ref. 40)	0.154	(0.646, 0.549, 0.549)	(0.555, 0.397, 0.397)	0.07	0.11
Experiment (Refs. 4, 8, and 9)	0.16			0.07	0.09
This study (no $p_{1/2}$ correction)	0.13	(0.667, 0.571, 0.571)	(0.667, 0.571, 0.571)	0.06	0.08
This study (with $p_{1/2}$ correction)	0.07	(0.667, 0.571, 0.571)	(0.571, 0.571, 0.429)	0.02	0.03

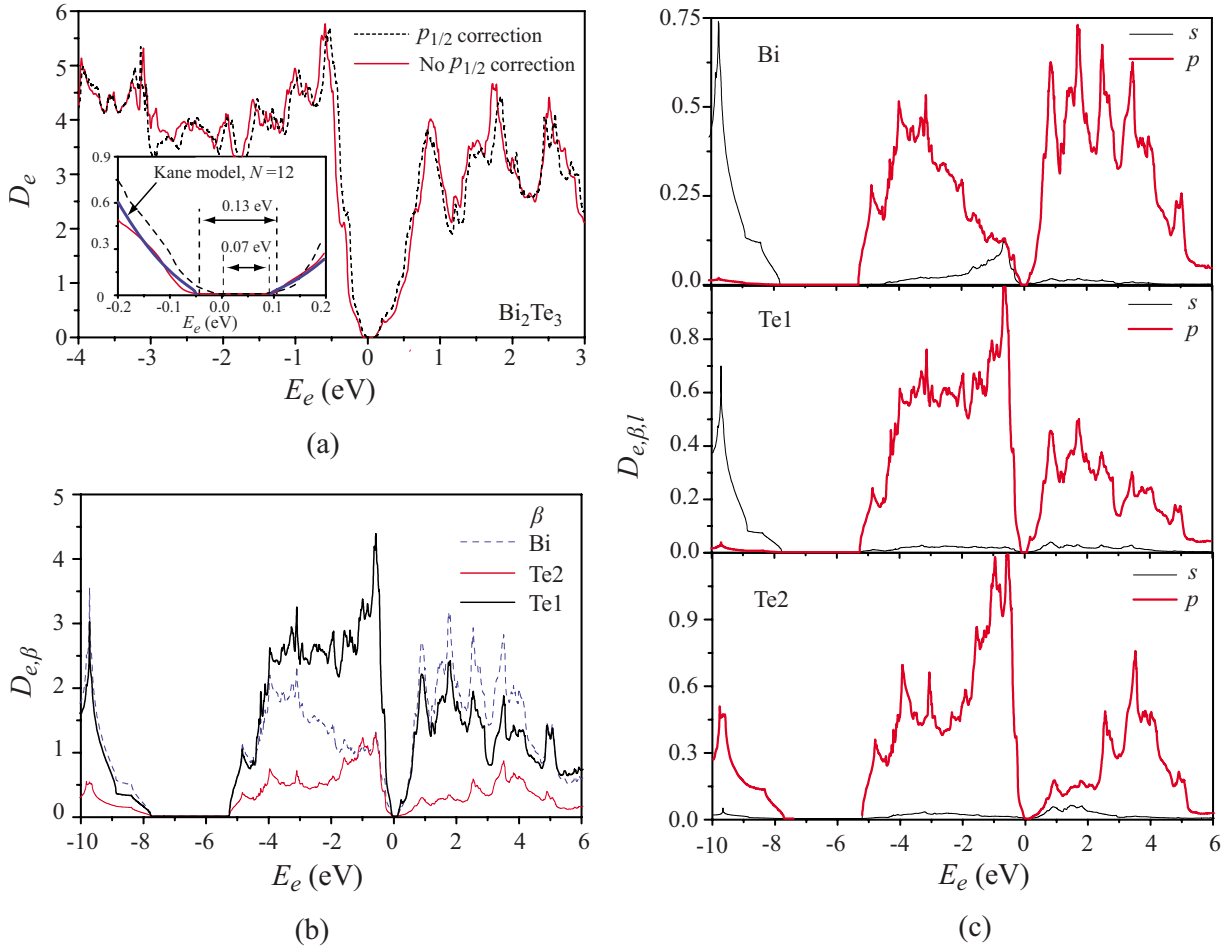

FIG. 9. (Color online) (a) Dimensionless electronic density of states D_e of Bi_2Te_3 with and without the $p_{1/2}$ corrections. The inset is for the band edge; also shown is D_e calculated by the Kane model. (b) Total $D_{e,\beta}$ for individual species β (partial D_e of each species times its multiplicity). (c) Decomposed, partial $D_{e,\beta,l}$ for each species.

$$E_e\left(1+\frac{E_e}{\Delta E_{e,g}}\right)=\frac{\hbar^2\kappa^2}{2m_{i,e,o}}, \tag{25}$$

where $m_{i,e,o}$ is the density of state effective mass at the band edge, $\Delta E_{e,g}$ is the energy gap, and κ is the wave vector. Note that here E_e is measured from the band edge. Then, the density of states D_e can be explicitly written as

$$D_e(E)=\frac{2^{1/2}Nm_{e,e,o}^{3/2}}{\pi^2\hbar^3}E_e^{1/2}\left(1+\frac{E_e}{\Delta E_{e,g}}\right)^{1/2}\left(1+2\frac{E_e}{\Delta E_{e,g}}\right). \tag{26}$$

Here, N is the multiplicity of the valleys. However, for Bi_2Te_3, it is D_e calculated by the Kane model using $N=12$ instead of $N=6$ that can match the results near the band edge from WIEN2K [shown in Fig. 9(a)]. This is believed to result from the secondary band edges, of which the energy only slightly differs from that of the band edges. This also leads to the total effective masses $m_{e,e}=N^{2/3}m_{e,e,o}=0.31m_e$ and $m_{h,e}=0.42m_e$ (m_e is the mass of a free electron), which agree well with $m_{e,e}=0.32m_e$ and $m_{h,e}=0.46m_e$ measured by Harman *et al.*[43] Also note that the energy regime in which the Kane model can provide a good approximation for D_e is within 0.1 eV around the band edges. Since only the states with an energy within $3k_BT$ about the chemical potential are important for the transport properties, the Kane model is believed to be a good approximation for D_e over a wide temperature range.

The total density of states without the $p_{1/2}$ corrections for each species (a product of the partial D_e of each species and its multiplicity) is shown in Fig. 9(b). For a comparison of the contributions of different orbitals, the orbital-decomposed D_e (without the $p_{1/2}$ corrections) are also shown in Fig. 9(c).

As shown in Fig. 9(b), for the valence bands, Te1 atoms contribute the most to the electronic density of states D_e near the band edge, while the contributions from Bi and Te2 atoms are less and nearly the same. This indicates that the Te1 atoms are probably going to lose electrons and be a donor in the structure. In contrast, for the conduction bands, the Bi atoms contribute the most to the density of states near the band edge, indicating that they are probably going to receive an electron and be an acceptor. Note that the contributions from Te1 atoms are only slightly less than those from the Bi atoms. This is consistent with the slightly ioniclike bond between the Bi and Te1 atoms. Te2 atoms contribute the least to

the density of states at both the valence and conduction band edges, indicating that they are relatively inert in determining the electronic transport properties of Bi_2Te_3. Figure 9(c) shows that for Te1 and Te2 atoms, p-type orbitals predominate in both valence and conduction bands. Bi atoms, however, have a strong $s+p$ orbital contribution at the valence band edge, but the wave function at the conduction band edge is mainly p type. Considering the layer sequence Te1-Bi-Te2-Bi-Te1, it seems that the bonds between the nearest-neighboring atoms in each quintuple layer are primarily the $pp\sigma$ interactions, as suggested by Mishra *et al.*[44]

B. Chemical potential

In a thermal equilibrium system, chemical potential μ is an essential parameter to describe the equilibrium distribution of carriers and their concentrations. All the electronic transport coefficients, in fact, are functions of the band structure $E_e(\boldsymbol{\kappa})$, μ, and temperature.

Generally, μ can be determined from

$$n_{d,h} - n_{d,e} = n_h + n_{h,b} - n_e - n_{e,b}, \tag{27}$$

where $n_{d,h}$ and $n_{d,e}$ are the concentrations of acceptors and donors, n_h is the hole concentration, $n_{h,b}$ is the concentration of holes bound on the acceptors, n_e is the electron concentration, and $n_{e,b}$ is the concentration of electrons bound on the donors. For modest doped semiconductors, $n_{h,b}$ and $n_{e,b}$ are normally negligible at normal and high temperatures (>100 K). Therefore, we can rewrite Eq. (27) as

$$n_{d,h} - n_{d,e} = \int_{-\infty}^{0} D_e(E_e) \frac{1}{e^{(\mu - E_e)/k_B T} + 1} dE_e - \int_{\Delta E_{e,g}}^{\infty} D_e(E_e) \frac{1}{e^{(E_e - \mu)/k_B T} + 1} dE_e. \tag{28}$$

Given $n_{d,h} - n_{d,e}$ and using the D_e calculated by the Kane model, we obtain the carrier concentrations and the chemical potentials at each temperature point. Figure 10 shows the temperature dependence of the calculated carrier concentrations and chemical potentials, compared with the experimental results[45] for p-type Bi_2Te_3 single crystals, where $n_{d,h} - n_{d,e} = 1.1 \times 10^{19}$ 1/cm^3. Both a constant $\Delta E_{e,g}$ and a temperature-dependent $\Delta E_{e,g}(T)$ were adopted in the calculation. As shown in Fig. 10, a constant $\Delta E_{e,g}$ gives a much lower carrier concentration compared to the experiments[45] at high temperatures ($T > 300$ K) when the thermal excitation of carriers becomes important. A good overall agreement can only be achieved by using a temperature-dependent band gap $\Delta E_{e,g} = 0.13 - 1.08 \times 10^{-4} T$. The different $\Delta E_{e,g}$ produce two chemical potential μ curves. The deviation between them is small under 200 K but becomes more prominent when $T \geqslant 250$ K, especially when $T \geqslant 500$ K. Below 300 K, μ resides within the valence band, and the sample is in the extrinsic regime. For $T > 300$ K, increasingly more carriers are thermally excited, leading μ into the band gap, and the crystal becomes intrinsic. At even higher temperatures, μ tends to move toward the middle of the band gap. In the following electrical transport calculations, we use μ calculated from Eq. (28) with the temperature-dependent $\Delta E_{e,g}$ by shifting the conduction band.

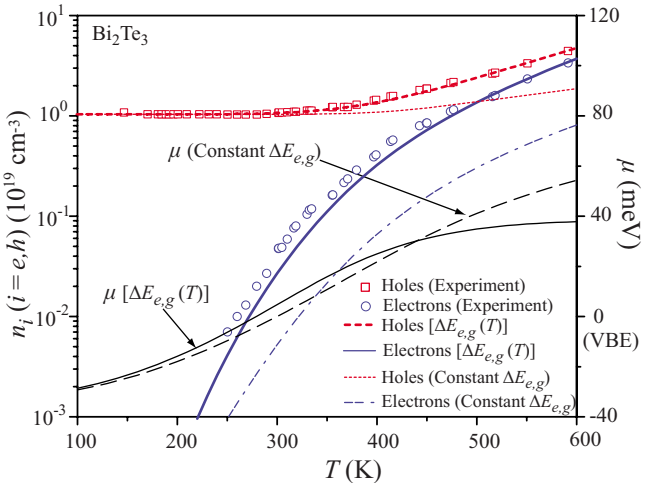

FIG. 10. (Color online) Temperature dependence of the calculated carrier concentrations and chemical potentials, compared with the experimental results (Ref. 45). Both a constant band gap $\Delta E_{e,g} = 0.13$ eV and a temperature-dependent band gap $\Delta E_{e,g} = 0.13 - 1.08 \times 10^{-4} T$ were used.

C. Relaxation-time models

The relaxation-time models simplify the calculation of BTE but condense all the complexities into the relaxation time τ_e. In principle, the scattering relaxation time can be obtained using the Fermi golden rule and the perturbation theory. The scattering of electrons is related to the perturbation of the Hamiltonian for an electron,[36,46]

$$H = -\frac{\hbar^2}{2m_e}\nabla^2 + \frac{e_c^2}{4\pi\epsilon_o}\int \frac{n_e g_e(\boldsymbol{r}')}{|\boldsymbol{r} - \boldsymbol{r}'|} d\boldsymbol{r}' + \varphi_{ec} + \varphi_{ext} + H', \tag{29}$$

$$H' = H'_{e-p,A} + H'_{e-p,O} + H'_{e-p,\mathrm{PO}} + H'_{e-v,d} + H'_{e-v,C} + \cdots = \varphi_{d,a}\frac{\partial \boldsymbol{d}}{\partial \boldsymbol{r}} + \varphi_{d,o}\boldsymbol{d} - \frac{e_c q_e}{V_o}\sum_{\kappa_p} \frac{\kappa_p}{\kappa_p^2 + \lambda^{-2}}(iQ_{\boldsymbol{\kappa}_p} e^{i\boldsymbol{\kappa}_p \cdot \boldsymbol{r}}) + \varphi_{v,c} + \frac{Ze_c^2}{4\pi\epsilon r} e^{-r/\lambda} + \cdots \tag{30}$$

where $g_e(\boldsymbol{r})$ is the electron radial distribution function, φ_{ec} is the exchange-autocorrelation energy, φ_{ext} is the external potential excluding the perturbation, H' is the perturbation Hamiltonian due to scatterings, $H'_{e-p,A}$, $H'_{e-p,O}$, $H'_{e-p,\mathrm{PO}}$, $H'_{e-v,d}$, and $H'_{e-v,C}$ are the perturbation Hamiltonian for the acoustic phonon scattering, nonpolar-optical phonon scattering, polar-optical phonon scattering, short-range scattering by impurity, and scattering by Coulomb potential, respectively. Here, $\varphi_{d,a}$ and $\varphi_{d,o}$ are the deformation potentials for the acoustic and optical phonons, q_e is the effective charge, and $\varphi_{v,c}$ is the scattering potential of impurity. $\boldsymbol{d} = N^{-1/2}\Sigma_{\boldsymbol{\kappa}_p} Q_{\boldsymbol{\kappa}_p} \boldsymbol{s}_{\boldsymbol{\kappa}_p} \exp(i\boldsymbol{\kappa}_p \cdot \boldsymbol{R})$ (N is the number of unit cells

and $\boldsymbol{s}_{\kappa_p}$ is the polarization vector) is the normal coordinate form of lattice displacement, $\boldsymbol{\kappa}_p$ is the phonon wave vector, $Q_{\boldsymbol{\kappa}_p}$ is the normal coordinate, λ is the screening length, and Ze_c' is the effective charge of impurity.

The electron relaxation time τ_e for mode $\boldsymbol{\kappa}$ can be represented as[46]

$$\frac{1}{\tau_e(\boldsymbol{\kappa})} = \sum_i \frac{1}{\tau_{e,i}(\boldsymbol{\kappa})} = \int \frac{d\boldsymbol{\kappa}'}{(2\pi)^3} \dot{\gamma}_{\boldsymbol{\kappa},\boldsymbol{\kappa}',i} \left(1 - \frac{g_{\boldsymbol{\kappa}'}}{g_{\boldsymbol{\kappa}}} \frac{f^o_{\boldsymbol{\kappa}}}{f^o_{\boldsymbol{\kappa}'}}\right), \tag{31}$$

where $f^o_{\boldsymbol{\kappa}}$ is the carrier equilibrium distribution, $g_{\boldsymbol{\kappa}}=f_{\boldsymbol{\kappa}}-f^o_{\boldsymbol{\kappa}}$ is the perturbation of the distribution, and $\dot{\gamma}_{\boldsymbol{\kappa},\boldsymbol{\kappa}',i}$ is the transition rate from state $\boldsymbol{\kappa}$ to $\boldsymbol{\kappa}'$ by the ith scattering, which can, in turn, be given by the Fermi golden rule as[46]

$$\dot{\gamma}_{\boldsymbol{\kappa},\boldsymbol{\kappa}',i} = \frac{2\pi}{\hbar} \delta[E_e - E_e(\boldsymbol{\kappa}')] |M_{\boldsymbol{\kappa},\boldsymbol{\kappa}',i}|^2,$$

$$M_{\boldsymbol{\kappa},\boldsymbol{\kappa}',i} = \langle \boldsymbol{\kappa}' | H_i' | \boldsymbol{\kappa} \rangle = \int \psi^\dagger(\boldsymbol{\kappa}', \boldsymbol{r}) H_i' \psi(\boldsymbol{\kappa}, \boldsymbol{r}) d\boldsymbol{r}, \tag{32}$$

where H_i' is the perturbation Hamiltonian for the scattering mechanism i and $\psi(\boldsymbol{\kappa},\boldsymbol{r})$ is the wave function for mode $\boldsymbol{\kappa}$. The Bloch wave function corresponding to the electron wave vector $\boldsymbol{\kappa}$ can be written as

$$\psi(\boldsymbol{\kappa}', \boldsymbol{r}) = \frac{1}{V^{1/2}} \sum_o C_J' \sum_{\boldsymbol{G}} C_{\boldsymbol{G}}^{\boldsymbol{\kappa}} e^{i(\boldsymbol{\kappa}+\boldsymbol{G})\cdot\boldsymbol{r}}, \tag{33}$$

where V is the volume, C and C' are coefficients, and the subscripts J and $\boldsymbol{G}$ denote the different orbitals and reciprocal lattice vectors, respectively. Therefore,

$$M_{\boldsymbol{\kappa},\boldsymbol{\kappa}'} = \frac{1}{V^{1/2}} \sum_{J'} \sum_J C_{J'}'^\dagger C_J' \sum_{G'} \sum_G e^{i(-\boldsymbol{\kappa}'-\boldsymbol{G}')\cdot\boldsymbol{r}} H' e^{i(\boldsymbol{\kappa}+\boldsymbol{G})\cdot\boldsymbol{r}}. \tag{34}$$

If the wave function and the perturbation potential can be obtained from the first-principles calculation, $\tau_{e,i}$ can be directly determined. This calculation is very challenging, and here we just introduce an analytical relaxation-time model, which is also based on the Fermi golden rule and incorporates the nonparabolic Kane model for energy dispersion.

Five common electron scattering mechanisms are considered in this work, namely, the deformation potential of the acoustic phonons $\tau_{e-p,A}$, deformation potential of the optical phonons $\tau_{e-p,O}$, polar scattering by the optical phonons $\tau_{e-p,\mathrm{PO}}$, short-range deformation potential of vacancies $\tau_{e-v,d}$, and Coulomb potential of vacancies $\tau_{e-v,C}$. According to the Matthiessen rule, the total scattering relaxation time τ_e is expressed as

$$\frac{1}{\tau_e} = \frac{1}{\tau_{e-p,A}} + \frac{1}{\tau_{e-p,O}} + \frac{1}{\tau_{e-p,\mathrm{PO}}} + \frac{1}{\tau_{e-v,d}} + \frac{1}{\tau_{e-v,C}}. \tag{35}$$

Using the Kane model, the expressions for the different scattering mechanisms are given as follows.[6]

(i) *Scattering by deformation potential of acoustic phonons* $\tau_{e-p,A}$. The relaxation time for electrons dispersed on the deformational potential of acoustic phonons, when using the Kane model of dispersion and assuming an elastic procedure, can be given as

$$\tau_{e-p,A} = \frac{(\tau_{e-p,A})_o \left(E_e + \frac{E_e^2}{\Delta E_{e,g}}\right)^{-1/2}}{\left(1 + 2\frac{E_e}{\Delta E_{e,g}}\right)[(1-A)^2 - B]},$$

$$A \equiv \frac{\frac{E_e}{\Delta E_{e,g}}(1-a_A)}{\left(1 + 2\frac{E_e}{\Delta E_{e,g}}\right)}, \quad a_A = \frac{\varphi_{d,A,v}}{\varphi_{d,A,c}},$$

$$B \equiv \frac{8\frac{E_e}{\Delta E_{e,g}}\left(1 + \frac{E_e}{\Delta E_{e,g}}\right)a_A}{3\left(1 + 2\frac{E_e}{\Delta E_{e,g}}\right)^2},$$

$$(\tau_{e-p,A})_o \equiv \frac{2\pi\hbar^4 C_l}{\varphi_{d,a,c}^2 k_B T (2m_{e,e,o})^{3/2}}, \tag{36}$$

where $\varphi_{d,A,c}$ is the acoustic deformation potential coupling constant for the conduction band, C_l is the combination of elastic constants, a_A is the ratio of the acoustic deformation potential coupling constants for the valence and conduction bands, and $m_{e,e,o}$ is the density of state effective mass for a single ellipsoid.

(ii) *Scattering by deformation potential of optical phonons* $\tau_{e-p,O}$

$$\tau_{e-p,O} = \frac{(\tau_{e-p,O})_o \left(E_e + \frac{E_e^2}{\Delta E_{e,g}}\right)^{-1/2}}{\left(1 + 2\frac{E_e}{\Delta E_{e,g}}\right)[(1-A)^2 - B]},$$

$$A \equiv \frac{\frac{E_e}{\Delta E_{e,g}}(1-a_O)}{\left(1 + 2\frac{E_e}{\Delta E_{e,g}}\right)}, \quad a_O = \frac{\varphi'_{d,O,v}}{\varphi'_{d,O,c}},$$

$$B \equiv \frac{8\frac{E_e}{\Delta E_{e,g}}(1 + E_e/\Delta E_{e,g})a_O}{3\left(1 + 2\frac{E_e}{\Delta E_{e,g}}\right)^2},$$

$$(\tau_{e-p,O})_o \equiv \frac{2\hbar^2 a^2 \rho (\hbar\omega_{p,O})^2}{\pi \varphi'^2_{d,o,c} k_B T (2m_{e,e,o})^{3/2}}, \tag{37}$$

where a is the lattice constant, ρ is the density, $\omega_{p,O}$ is the frequency of the optical phonons, a_O is the ratio of the optical deformation potential coupling constants for valence and conduction bands.

(iii) *Scattering by polar-optical phonons* $\tau_{e-p,\mathrm{PO}}$. In a simple isotropic parabolic model, the relaxation time for po-

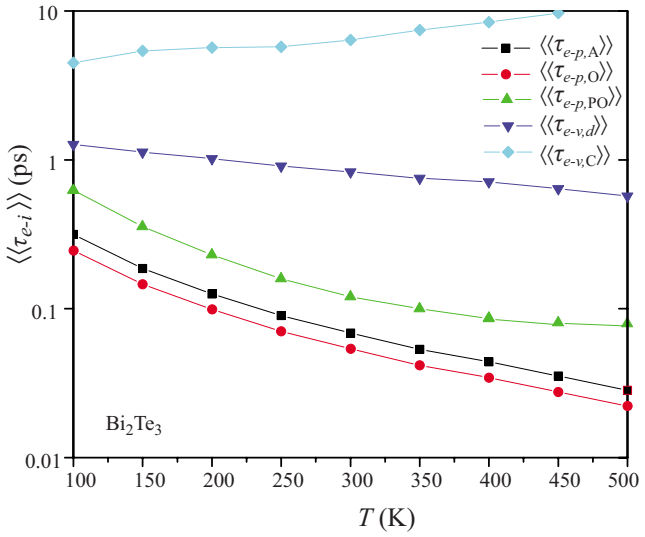

FIG. 11. (Color online) Variation of calculated average electron relaxation times for Bi_2Te_3 with respect to temperature using the Kane band model for energy dispersion.

lar longitudinal optical phonons has the form

$$\tau_{e-p,\mathrm{PO}}^{-1} \sim \frac{1}{u_e \kappa^2} \int_0^{2\kappa} q dq, \tag{38}$$

where u_e is the velocity of electrons. When the integral takes into account all phonons, we have

$$\tau_{e-p,\mathrm{PO}} = \frac{\hbar^2 u_e}{2k_B T e_c^2 [(\epsilon_o \epsilon_{e,s})^{-1} - (\epsilon_o \epsilon_{e,\infty})^{-1}]}. \tag{39}$$

Inclusion of nonparabolicity and screening effects will lead to

$$\tau_{e-p,\mathrm{PO}} = \frac{\hbar^2 \left(E_e + \frac{E_e^2}{\Delta E_{e,g}}\right)^{1/2} F^{-1}}{e_c^2 (2m_{e,e,o})^{1/2} k_B T [(\epsilon_o \epsilon_{e,s})^{-1} - (\epsilon_o \epsilon_{e,\infty})^{-1}] \left(1 + 2\frac{E_e}{\Delta E_{e,g}}\right)},$$

$$F \equiv 1 - \delta \ln(1 + \delta^{-1}) - \frac{2\frac{E_e}{\Delta E_{e,g}}\left(1 + \frac{E_e}{\Delta E_{e,g}}\right)}{\left(1 + 2\frac{E_e}{\Delta E_{e,g}}\right)^2} \times [1 - 2\delta + 2\delta^2 \ln(1 + \delta^{-1})],$$

$$\delta \equiv (2\kappa \lambda_o)^{-2}, \tag{40}$$

where $\epsilon_{e,s}$ and $\epsilon_{e,\infty}$ are the static and high-frequency relative permitivities, κ is the carrier wave vector, and λ_o is the screening length of the optical phonons.

(iv) *Scattering by short-range deformation potential of vacancies* $\tau_{e-v,d}$. $\tau_{e-v,d}$ also has a form similar to the relaxation time of electron-acoustic phonon scattering due to a similar deformation potential, which is

$$\tau_{e-v,d} = \frac{(\tau_{e-v,d})_o \left(E_e + \frac{E_e^2}{\Delta E_{e,g}}\right)^{-1/2}}{\left(1 + 2\frac{E_e}{\Delta E_{e,g}}\right)[(1-A)^2 - B]},$$

$$A \equiv \frac{\frac{E_e}{\Delta E_{e,g}}(1 - a_v)}{\left(1 + 2\frac{E_e}{\Delta E_{e,g}}\right)}, \quad a_v = \frac{\varphi'_{v,v}}{\varphi'_{v,c}},$$

$$B \equiv \frac{8\frac{E_e}{\Delta E_{e,g}}(1 + E_e/\Delta E_{e,g}) a_v}{3\left(1 + 2\frac{E_e}{\Delta E_{e,g}}\right)^2},$$

$$(\tau_{e-v,d})_o \equiv \frac{\pi \hbar^4}{\varphi'^2_{v,c} m_{e,e,o} (2m_{e,e,o})^{1/2} n_v}, \tag{41}$$

where n_v is the vacancy density and a_v is the ratio of the short-range deformation potential coupling constants of vacancies for valence and conduction bands.

(v) *Scattering by Coulomb potential of vacancies* $\tau_{e-v,C}$

$$\tau_{e-v,C} = \frac{\epsilon_s^2 (2m_{e,e,o})^{1/2} \left(E_e + \frac{E_e^2}{\Delta E_{e,g}}\right)^{3/2}}{\pi (z e_c^2)^2 n_v [\ln(1 + \xi) - \xi/(1 + \xi)] \left(1 + 2\frac{E_e}{\Delta E_{e,g}}\right)},$$

$$\xi \equiv (2\kappa \lambda_v)^2, \tag{42}$$

where ze_c is the vacancy charge and λ_v is the screening radius of the vacancy potential and is given as

$$\lambda_v^{-2} = \frac{4\pi e_c^2}{\epsilon_s} D_e(\mu), \quad \mu = E_F,$$

$$D_e(\mu) \equiv \frac{2^{1/2} (m_{e,e,o})^{3/2}}{\pi^2 \hbar^3} \left(\mu + \frac{\mu^2}{\Delta E_{e,g}}\right)^{1/2} \left(1 + 2\frac{\mu}{\Delta E_{e,g}}\right), \tag{43}$$

where $D_e(\mu)$ is actually the density of states at the Fermi level.

Figure 11 shows the temperature dependence of the calculated average relaxation times described above. The parameters used in the calculation are listed in Table V. Some parameters, e.g., the deformation potentials, are obtained by fitting the electrical conductivity with experimental results at 100 K. Overall, the scatterings by acoustic and optical phonons dominate the electrical transport of Bi_2Te_3. On the other hand $\langle\langle \tau_{e-v,d} \rangle\rangle$ and $\langle\langle \tau_{e-v,C} \rangle\rangle$ are orders of magnitudes larger than $\langle\langle \tau_{e-p,A} \rangle\rangle$ and $\langle\langle \tau_{e-p,O} \rangle\rangle$. Therefore, the scatterings by the short-range deformation potential of vacancies and Coulomb potentials are unimportant for the electrical transport of Bi_2Te_3. Note that $\langle\langle \tau_{e-p,\mathrm{PO}} \rangle\rangle$ is comparable with $\langle\langle \tau_{e-p,A} \rangle\rangle$ and $\langle\langle \tau_{e-p,O} \rangle\rangle$. Therefore, the polar scattering by optical phonons is also important.

TABLE V. Parameters used in the relaxation-time models for Bi_2Te_3, from fit to experimental results (Ref. 45).

Parameter	Magnitude	Parameter	Magnitude
$m_{h,e,o}/m_e$	0.08	$m_{e,e,o}/m_e$	0.06
n_v $(1/m^3)$	1.04×10^{25}	ρ (kg/m^3)	7.86×10^3
$\epsilon_{e,o}$	400	$\epsilon_{e,\infty}$	69.8
C_l (N/m^2)	0.71×10^{11}	$\hbar\omega_o$ (eV)	0.0061
z	0.1	$\varphi_{d,A,c}$ (eV)	35
$\varphi_{d,O,c}$ (eV)	40	$\varphi'_{v,c}$ $(J\ m^3)$	1.2×10^{-46}
a_A, a_O, a_v	1.0	a (Å)	10.45
$\Delta E_{e,g}$ (eV)	$0.13-1.08\times10^{-4}T$		

D. Seebeck coefficient

Figure 12 shows the variation of calculated $\alpha_{S,\parallel}$ of Bi_2Te_3 with temperature using Eq. (24). The calculation was carried out using BOLTZTRAP, a software package adopting BTEs. Both the energy-dependent relaxation-time models (Sec. III E) and the constant relaxation-time model were used. We modified the BOLTZTRAP code and incorporated the relaxation-time model into the integration since BOLTZTRAP assumes a constant relaxation time. The corresponding Fermi energy at each temperature is determined by Eq. (28) along with the Kane band model for D_e. To incorporate the temperature dependence of the band structure, we assume that the band structure does not change with temperature and shifts the conduction band in the calculation to include the temperature dependence of the band gap $\Delta E_{e,g}$. Figure 12 shows that the constant $\Delta E_{e,g}$ leads to much higher values for $T>300$ K (intrinsic regime), while results calculated with the temperature-dependent $\Delta E_{e,g}=0.13-1.08\times10^{-4}T$ agree quite well with the experimental results. However, in the extrinsic regime ($T\leqslant300$ K), there is only minor difference between the results with the two different settings for $\Delta E_{e,g}$. As shown in Fig. 12, with the same temperature-dependent $\Delta E_{e,g}=0.13-1.08\times10^{-4}T$ eV, the two relaxation-time models give very similar results in the extrinsic regime since one kind of carriers dominates the electrical transport. However, some deviation appears in the intrinsic regime, where the concentrations of the holes and electrons become comparable, and it increases with increasing temperature. This phenomenon indicates that the temperature dependences of the mobilities of holes and electrons are different.

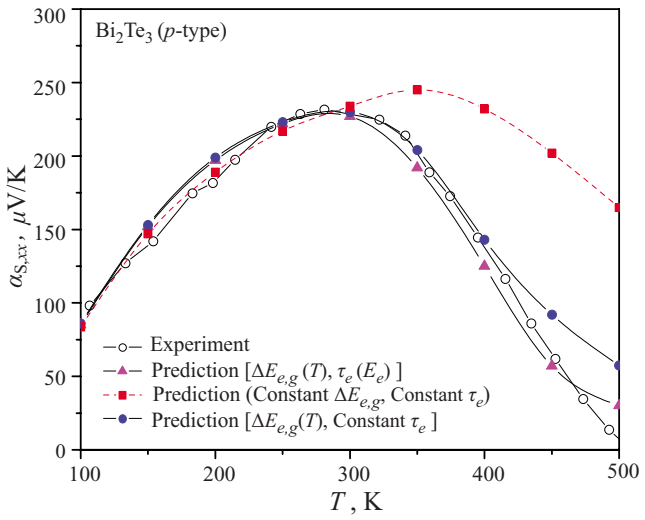

FIG. 12. (Color online) Variation of the calculated Seebeck coefficient for p-type Bi_2Te_3 with respect to temperature, compared with the available experimental results (Ref. 45). Both a temperature-dependent band gap $\Delta E_{e,g}=0.13-1.08\times10^{-4}T$ eV and a constant $\Delta E_{e,g}=0.13$ eV are used. Also shown are the predictions using the energy-dependent relaxation times and the constant relaxation-time model.

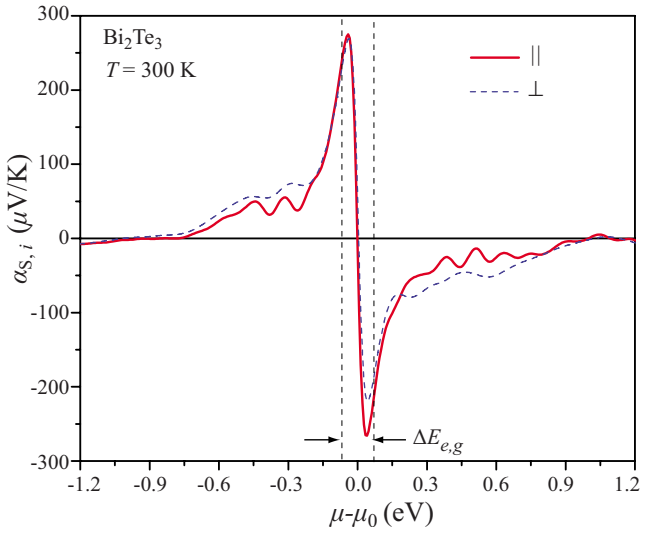

FIG. 13. (Color online) Variation of the calculated Seebeck coefficient of Bi_2Te_3 at $T=300$ K with respect to the chemical potential μ.

The band structure calculated with the experimental lattice parameters at 300 K was used in the above calculations for α_S. Temperature changes not only the carrier concentrations but also the lattice parameters. However, the band structure calculations adopting the lattice parameters under different temperatures show that the thermal expansion has negligible effects on the band structure. The change of lattice parameters from 0 to 300 K only results in a less than 2% change in the band gap. Compared with the actual temperature dependence of band gap,[47] it seems that the temperature variation of the band gap is mainly due to lattice vibration.

Figure 13 shows the variation of α_S along the $\parallel$ and $\perp$ directions, with respect to the chemical potential μ, at 300 K. Apparently, the two curves are very similar, indicating the isotropy of α_S. Figure 13 shows that for p-type Bi_2Te_3, the α_S peaks along the $\parallel$ and $\perp$ directions almost overlap. However, for n-type Bi_2Te_3, the absolute peak value α_S along the $\parallel$ direction is larger than that along the $\perp$ direction, though the peak positions are identical. In Fig. 13, μ_0 is the chemical potential value at which $\alpha_S=0$. It is useful to rewrite the relation for α_S in Eq. (24) as

$$\alpha_S = \frac{k_B}{e_c}\frac{\langle E_e-\mu\rangle_{\sigma_e(E_e,\mu)}}{k_BT},$$

$$\langle E_e-\mu\rangle_{\sigma_e(E_e,\mu)}=\frac{\int\sigma_e(E_e,\mu)(E_e-\mu)dE_e}{\int\sigma_e(E_e,\mu)dE_e}. \quad (44)$$

Here, $\langle E_e-\mu\rangle_{\sigma_e(E_e,\mu)}$ is the $\sigma_e(E_e,\mu)$-averaged energy deviation from the chemical potential. Then, we have

$$\mu_0=\langle E_e\rangle_{\sigma_e(E_e,\mu_0)}, \quad (45)$$

which is the $\sigma_e(E_e)$-averaged energy close to the middle of the band gap. Therefore,

$$\alpha_S=\frac{k_B}{e_c}\frac{[\langle E_e\rangle_{\sigma_e(E_e,\mu)}-\langle E_e\rangle_{\sigma_e(E_e,\mu_0)}]-(\mu-\mu_0)}{k_BT}. \quad (46)$$

$\langle E_e\rangle_{\sigma_e(E_e,\mu)}$ has a simple form if the nondegenerate approximation may be used, that is,

$$\langle E_e\rangle_{\sigma_e(E_e,\mu)}\simeq\frac{\sigma_{e,e}\Delta E_{e,g}}{\sigma_{e,e}+\sigma_{e,h}}=\frac{1}{1+be^{-2\epsilon/(k_BT)}}\Delta E_{e,g}, \quad (47)$$

where $\sigma_{e,e}$ and $\sigma_{e,h}$ are the electrical conductivity contributed by electrons and holes, $b=(\mu_h/\mu_e)(m_{e,h}/m_{e,e})^{3/2}$ (μ_h and μ_e are the mobilities of electrons and holes), and $\Delta E_e=\mu-\Delta E_{e,g}/2$ is the separation of the chemical potential above the middle of the band gap. Apparently, for semiconductors with a large band gap (e.g., $\Delta E_{e,g}>10k_BT$), the absolute value of the maximum α_S can be estimated as

$$|\alpha_{S,max}|=\frac{k_B}{|e_c|}\frac{\Delta E_{e,g}}{2k_BT}. \quad (48)$$

For small $2\Delta E_e/k_BT$, we have

$$\langle E_e\rangle_{\sigma_e(E_e,\mu)}\simeq\frac{\Delta E_{e,g}}{1+b}\left[1+\frac{2b\Delta E_e/(k_BT)}{1+b}\right]. \quad (49)$$

Therefore,

$$\alpha_S\simeq\frac{k_B}{e_c}\frac{\left[\frac{2b\Delta E_{e,g}}{(1+b)^2k_BT}-1\right](\mu-\mu_0)}{k_BT}. \quad (50)$$

For narrow band-gap semiconductors, as shown in Fig. 13, Eq. (50) is a good approximation for α_S when $|\mu-\mu_0|<\Delta E_{e,g}/2$. When μ moves toward the band edge, the effects of opposite charges become smaller; when μ moves further into the band edge, $\langle E_e\rangle_{\sigma_e(E_e,\mu)}$ will become closer to μ. Therefore, α_S will achieve the maximum near the band edge, and the maximum value can be estimated from Eq. (50). Assuming that $b=1$ and the maximum is achieved at the band edge for Bi_2Te_3 at 300 K, $|\alpha_S|_{max}\simeq 320$ μV/K, close to the maximum in Fig. 13.

E. Electrical conductivity and electric thermal conductivity

Figure 14 shows the calculated electrical conductivity of Bi_2Te_3 along the $\parallel$ and $\perp$ directions, wherein the Kane band model based relaxation times are used. The temperature-dependent band gap $\Delta E_{e,g}=0.13-1.08\times10^{-4}T$ eV and the corresponding chemical potential calculated in Sec. III B are adopted in the calculation. The parameters for the relaxation-time models are listed in Table V. Below 300 K, the ratio

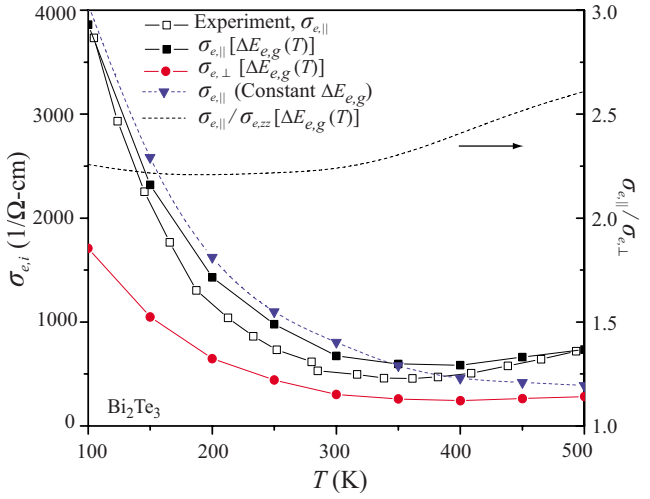

FIG. 14. (Color online) Variation of calculated directional electrical conductivity for Bi_2Te_3 with respect to temperature using the Kane band model and energy-dependent relaxation times, and comparison with the available experimental results (Ref. 45).

$\sigma_{e,\parallel}/\sigma_{e,\perp}$ is around 2.2 and is almost temperature independent. However, above 300 K, $\sigma_{e,\parallel}/\sigma_{e,\perp}$ increases with increasing temperature. From the results shown in Fig. 14, this is because $\sigma_{e,\parallel}$ changes much faster than $\sigma_{e,\perp}$ at high temperatures. Note that the calculated $\sigma_{e,\parallel}/\sigma_{e,\perp}$ is lower than the experimental values [around 2.95 (Ref. 48)]. The deviation is caused probably by neglecting the directional dependence of the effective masses.

We also used a constant band gap $\Delta E_{e,g}=0.13$ eV for the calculation of σ_e using the above energy-dependent relaxation-time models. The same parameters in Table V are used, and the results are also plotted in Fig. 14. Below 300 K, the $\sigma_{e,\parallel}$ calculated with a constant $\Delta E_{e,g}$ is fairly close to those results with a temperature-dependent $\Delta E_{e,g}(T)$. However, in the intrinsic regime, the larger band gap suppresses the thermal excitation of carriers and thus leads to lower σ_e values. Note that with a constant $\Delta E_{e,g}$, $\sigma_{e,\parallel}$ continues to decay without any rebound shown in the experimental results. However, a temperature-dependent $\Delta E_{e,g}(T)$ yields a much better agreement with the experiments at high temperatures, indicating that the temperature dependence of the band gap is important in predicting the temperature dependence of the electrical conductivity.

Traditionally, the Wiedemann-Franz Law, $k_e=N_L\sigma_eT$, where N_L is the Lorenz number, is used to calculate the electric thermal conductivity k_e on the basis of σ_e. However, for semiconductors, N_L may not be the values used for metals $[N_{L,o}=(\pi^2/3)k_B^2/e_c^2]$, especially when the chemical potential is near the center of the band gap.[49] Figure 15(a) shows the variation of the directly calculated Lorenz number N_L (scaled with $N_{L,o}$) for Bi_2Te_3 (along $\parallel$ and $\perp$) at 300 K, with respect to the chemical potential. The results are similar to those found by Chaput *et al.*[49] for doped skutterudites. When the sample is heavily doped (the chemical potential is deep inside the valence or conduction band), $N_L/N_{L,o}$ is close to 1.0. However, for intermediate doping, $N_L/N_{L,o}$ can be smaller than 1.0, and the minimum is around 0.7. For small doping

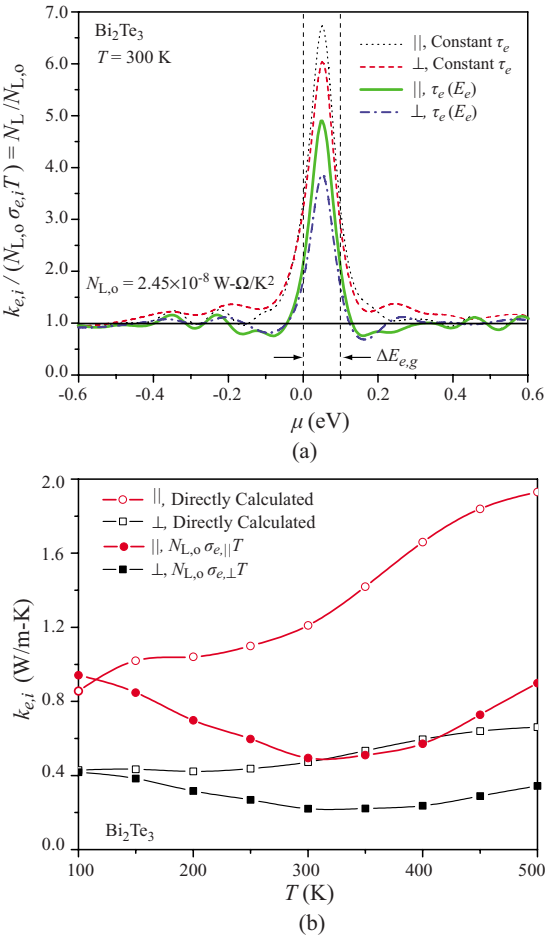

FIG. 15. (Color online) (a) Variation of the calculated scaled Lorenz number for Bi_2Te_3 (along ∥ and ⊥) with respect to the chemical potential. Both the constant relaxation-time model and the energy-dependent relaxation-time model (with the Kane band dispersion) results are shown. (b) Variation of the calculated k_e along the ∥ and ⊥ directions with respect to temperature. The results calculated using the constant $N_{L,o}$, i.e., $N_{L,o}\sigma_e T$, are also shown.

concentrations or intrinsic regime, $N_L/N_{L,o}$ may be much larger than 1.0. Figure 15(a) also shows that the constant relaxation-time model will lead to a larger N_L, compared to that for the energy-dependent relaxation-time model discussed above. For both relaxation-time models, N_L along the ∥ direction is slightly larger than that along the ⊥ direction. Figure 15(b) shows the temperature dependence of the electric thermal conductivity calculated according to Eq. (24) and that calculated from $N_{L,o}\sigma_e T$. The results from Eq. (24) show that k_e for both directions increase with increasing temperature, while $N_{L,o}\sigma_e T$ results show valleys near the room temperature. Due to the significant changes of N_L in the intrinsic regime, $N_{L,o}\sigma_e T$ underestimates k_e at high temperatures.

F. Figure of merit

Figure 16 shows the variation of the figure of merit ZT for the p-type Bi_2Te_3 specimen of experiment[45] along the ∥ and ⊥ directions, with respect to temperature. The lower two

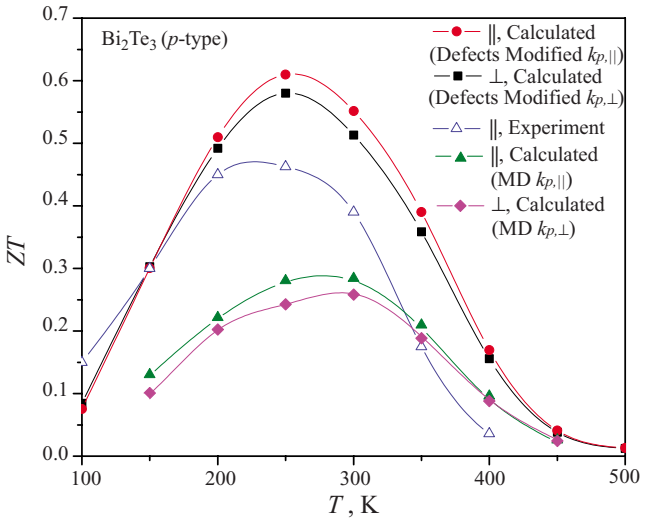

FIG. 16. (Color online) Variation of calculated directional figure of merit for Bi_2Te_3 (along ∥ and ⊥) with respect to temperature. Both the results with the directly calculated k_p and that modified by defects are presented. The experimental results (Ref. 45) are also shown.

curves are based on the directly (MD) calculated k_p. Since k_p and σ_e are very sensitive to defects, which are always present in fabricated specimens, for comparison between the calculated and measured ZT, we used a modified k_p, and the results are shown with the top two curves. Due to the difficulty in modeling various defects, the modified k_p was obtained by fitting the total thermal conductivity to the experimental results[45] at 300 K and then by using the $1/T$ law at other temperatures. The experimental results are also shown in Fig. 16. The ZT with a modified k_p is higher than experimental results above 200 K, mainly due to the overestimation of σ_e. The calculated ZT reaches its maximum at around 250 K. ZT along the ∥ direction is higher than that along the ⊥ direction between 200 and 400 K due to the larger ratio $\sigma_{e,\parallel}/\sigma_{e,\perp}$ compared to $k_{p,\parallel}/k_{p,\perp}$. Note that the experimental $\sigma_{e,\parallel}/\sigma_{e,\perp}$ is larger than the calculated results (discussed above), so the difference in the figure of merits along the ∥ and ⊥ direction is expected to be even larger.

IV. SUMMARY AND CONCLUSION

The interatomic potentials for Bi_2Te_3 have been developed, and the calculated elastic constants and thermal expansion coefficients agree well with the experimental data, indicating that the proposed force field is suitable in describing both the harmonic and anharmonic behaviors of Bi_2Te_3. The interaction between two Te1 atoms in the neighboring layers is a mixture of the electrostatic interaction and the van der Waals interaction and behaves like an ionic bond. The force constant difference between the Te1-Te1 and Te2-Bi bonds leads to a phonon band gap near 2.5 THz. There is only a small difference between the in-plane and cross-plane vibrations, and no significant two-dimensional elastic behavior has been found in this layered structure. However, the anisotropy in the polarized Grüneisen parameter shows much

stronger anharmonicity along the cross-plane direction, which is mainly due to the high anharmonic Te1-Te1 interaction.

The temperature dependence of the in-plane and cross-plane lattice thermal conductivities $k_{p,A,\parallel}$ and $k_{p,A,\perp}$ has been calculated in a temperature range from 150 to 450 K. The ratio $k_{p,A,\parallel}/k_{p,A,\perp}$ varies from 1.55 to 2.17 in this temperature regime. Since the elastic properties along the two directions are nearly the same, the difference between $k_{p,A,\parallel}$ and $k_{p,A,\perp}$ is believed to be mainly due to the different inharmonicity along the two directions. The calculated in-plane thermal conductivity roughly follows the $1/T$ law, while the calculated cross-plane lattice thermal conductivity seems to have a slightly stronger temperature dependence (i.e., $1/T^{1.23}$), which may be due to the larger thermal expansion effects along that direction. The decomposition of the lattice thermal conductivity shows that the long-range acoustic phonons dominate the heat transfer in both the in-plane and cross-plane directions. The contribution from the long-range acoustic phonons $k_{p,A,lg}$ has a strong temperature dependence; in contrast, the contribution from the short-range acoustic phonons $k_{p,A,sh}$ and that from the optical phonons $k_{p,O}$ are also temperature-independent. Also, at each temperature point, $k_{p,A,sh}$ and $k_{p,O}$ along the in-plane and cross-plane directions are almost identical. Therefore, $k_{p,A,sh}$ and $k_{p,O}$ are not sensitive to the inharmonicity. The sum of $k_{p,A,sh}$ and $k_{p,O}$ provides a lower limit for the doped bulk Bi_2Te_3, which is about 0.2 W/m K at 300 K. By using direction-dependent $T_{D,\infty}$ and γ_G, the Slack model was also extended for anisotropic materials. The extended Slack model gives a good estimation for both the in-plane and cross-plane lattice thermal conductivities, indicating that the phonon transport along a given direction is only affected by the elastic and inharmonic properties along that direction.

We have also calculated the temperature dependence of α_S, σ_e, and k_e over the temperature range from 100 to 500 K. These calculations are based on the band structure, μ, and τ_e. The Kane band model is found to be appropriate in describing the nonparabolicity of the Bi_2Te_3 band structure. The fitting with the carrier concentration and μ shows that the temperature dependence of the band gap is important to give a good prediction. The thermal expansion has negligible effects on the relationship between α_S and μ; therefore, the effects of temperature on α_S are mainly through changing the distribution function and μ. Both the constant relaxation-time model and the analytic relaxation-time model with the nonparabolic Kane model for energy dispersion have been used in the calculations for α_S. The results show that α_S is sensitive to the temperature dependence of the band gap and the relaxation time models in the intrinsic regime.

The fitting for σ_e using the relaxation-time model also shows that the polar scattering by optical phonons and the scattering by the deformation potential of acoustic and optical phonons predominate the electron transport in Bi_2Te_3. The scatterings by the short-range deformation potential of vacancies and the Coulomb potentials are negligible. The comparison of the temperature dependence of different scattering mechanisms also shows that the temperature dependence of the band gap is important in describing the temperature dependence of σ_e. It is also found that the Lorenz number can be smaller than the value for metals for intermediate doping and will become much larger in the intrinsic regime. In the relaxation-time models used, some parameters are found by fitting to the experimental data on σ_e. Further work will use the first-principles methods [e.g., Eq. (32)] to calculate the scattering rates by acoustic and optical phonons.

ACKNOWLEDGMENTS

This work was supported by the U.S. Department of Energy, Office of Basic Energy Sciences under Grant No. DE-FG02-00ER45851. Insightful discussions with S. M. Mahanti, Jasprit Singh, Ctirad Uher, and Anton Van der Ven have been very helpful.

*kaviany@umich.edu

[1] M. H. Francombe, Br. J. Appl. Phys. **9**, 415 (1958).
[2] J. R. Wiese and L. Muldawer, J. Phys. Chem. Solids **15**, 13 (1960).
[3] J. O. Jenkins, J. A. Rayne, and R. W. Ure, Phys. Rev. B **5**, 3171 (1972).
[4] H. J. Goldsmid, *Thermoelectric Refrigeration* (Plenum, New York, 1964).
[5] W. Kullmann, G. Eichhorn, H. Rauh, R. Geick, G. Eckold, and U. Steigenberger, Phys. Status Solidi B **162**, 125 (1990).
[6] D. M. Zayachuk, Semiconductors **31**, 173 (1997).
[7] D. L. Rode, Semicond. Semimetals **10**, 1 (1975).
[8] H. Kohler, Phys. Status Solidi B **74**, 591 (1976).
[9] H. Kohler, Phys. Status Solidi B **73**, 95 (1976).
[10] T. J. Scheidemantel, C. Ambrosch-Draxl, T. Thonhauser, J. V. Badding, and J. O. Sofo, Phys. Rev. B **68**, 125210 (2003).
[11] J. Callaway, Phys. Rev. **113**, 1046 (1959).
[12] M. G. Holland, Phys. Rev. **132**, 2461 (1963).
[13] S. Baroni *et al.*, http://www.pwscf.org/, 2007.
[14] J. Gale and A. Rohl, Mol. Simul. **29**, 291 (2003).
[15] H. Rydberg, M. Dion, N. Jacobson, E. Schröder, P. Hyldgaard, S. I. Simak, D. C. Langreth, and B. I. Lundqvist, Phys. Rev. Lett. **91**, 126402 (2003).
[16] N. W. Ashcroft and N. D. Mermin, *Solid State Physics* (Saunder College, Philadelphia, 1976).
[17] J. O. Barnes and J. A. Rayne, Phys. Lett. **46A**, 317 (1974).
[18] D. A. Broido, A. Ward, and N. Mingo, Phys. Rev. B **72**, 014308 (2005).
[19] R. R. Rao and A. Ramanand, Acta Crystallogr., Sect. A: Cryst. Phys., Diffr., Theor. Gen. Crystallogr. **A33**, 146 (1977).
[20] K. N. R. Taylor, Br. J. Appl. Phys. **12**, 717 (1961).
[21] B. L. Huang and M. Kaviany, J. Appl. Phys. **100**, 123507 (2006).
[22] M. T. Dove, *Introduction to Lattice Dynamics* (Cambridge University Press, Cambridge, England, 1993).
[23] Z. Yao, J. S. Wang, B. Li, and G. R. Liu, Phys. Rev. B **71**, 085417 (2005).

[24] H. Rauh, R. Geick, H. Kohler, N. Nucker, and N. Lehner, Solid State Phys. **14**, 2705 (1981).
[25] D. Wolf, P. Keblinski, S. R. Phillpot, and J. Eggebrecht, J. Chem. Phys. **110**, 8254 (1999).
[26] A. J. H. McGaughey and M. Kaviany, Int. J. Heat Mass Transfer **47**, 1799 (2004).
[27] C. B. Satterthwaite and J. R. W. Ure, Phys. Rev. **108**, 1164 (1957).
[28] P. A. Walker, Proc. Phys. Soc. London **76**, 113 (1960).
[29] B. L. Huang and M. Kaviany, Int. J. Heat Mass Transfer **50**, 393 (2007).
[30] H. Kaburaki, J. Li, S. Yip, and H. Kimizuka, J. Appl. Phys. **102**, 043514 (2007).
[31] D. G. Cahill, S. K. Watson, and R. O. Pohl, Phys. Rev. B **46**, 6131 (1992).
[32] G. A. Slack, Solid State Phys. **34**, 1 (1979).
[33] R. Berman, *Thermal Conduction in Solids* (Clarendon, Oxford, 1976).
[34] J. M. Ziman, *Electrons and Phonons* (Oxford University Press, London, 1962).
[35] G. K. H. Madsen and D. J. Singh, Comput. Phys. Commun. **175**, 67 (2006).
[36] P. Blaha, K. Schwarz, G. K. H. Madsen, D. Kvasnicka, and J. Luitz, *WIEN2k, An Augmented Plane* Wave+Local *Orbitals Program for Calculating Crystal Properties* (Karlheinz Schwarz, Technische Uniersitat Wien, Austria, 2001).
[37] J. P. Perdew, K. Burke, and M. Ernzerhof, Phys. Rev. Lett. **77**, 3865 (1996).
[38] P. Larson, Phys. Rev. B **68**, 155121 (2003).
[39] S. J. Youn and A. J. Freeman, Phys. Rev. B **63**, 085112 (2001).
[40] M. Kim, A. J. Freeman, and C. B. Geller, Phys. Rev. B **72**, 035205 (2005).
[41] E. O. Kane, Semicond. Semimetals **1**, 75 (1966).
[42] Y. I. Ravich, B. A. Efimova, and V. I. Tamachenko, Phys. Status Solidi B **43**, 11 (1971).
[43] T. C. Harman, B. Paris, S. E. Miller, and H. L. Goering, J. Phys. Chem. Solids **2**, 181 (1957).
[44] S. K. Mishra, S. Satpathy, and O. Jepsen, J. Phys.: Condens. Matter **9**, 461 (1997).
[45] H.-W. Jeon, H.-P. Ha, D.-B. Hyun, and J.-D. Shim, J. Phys. Chem. Solids **52**, 579 (1991).
[46] J. P. Singh, *Electronic and Optoelectrionic Properties of Semiconductor Structures* (Cambridge University Press, Cambridge, England, 2003).
[47] S. Shigetomi and S. Mori, J. Phys. Soc. Jpn. **11**, 915 (1956).
[48] R. T. Delves, A. E. Bowley, D. W. Hazelden, and H. J. Goldsmid, Proc. Phys. Soc. London **78**, 838 (1961).
[49] L. Chaput, P. Pecheur, J. Tobola, and H. Scherrer, Phys. Rev. B **72**, 085126 (2005).